Challenge Journal of STRUCTURAL MECHANICS

Vol.3 No.4 (2017)

North Anatolian Fault Zone Poisson method building codes columns continuous girder bridge corrosion durability dynamic analysis dynamic response earthquake earthquake hazard finite element analysis finite element method optimization reinforced concrete seismic analysis seismic design seismic isolation seismic response teaching-learning based optimization wind

TULPAR ACADEMIC PUBLISHING

ISSN 2149-8024

Challenge Journal of Structural Mechanics

E-mail: *cjsmec@challengejournal.com*

Web page: *cjsmec.challengejournal.com*

TULPAR Academic Publishing
www.tulparpublishing.com

Challenge Journal of Structural Mechanics

CONTENTS

A hybrid multi-objective algorithm to predict the characteristics of soil profiles from seismic ground motion records
Zamila Harichane, Mourad A. Khellafi, Amina Sadouki **138**

Estimating bearing capacity of shallow foundations by artificial neural networks
Mustafa Aytekin **151**

Mechanical and thermal behaviors comparison of basalt and glass fibers reinforced concrete with two different fiber length distributions
Sadık Alper Yıldızel **155**

Structural behaviour of concrete filled hollow steel sections exposed to parametric fire
Mohammed Salah Dimia, Soumia Sekkiou, Mohamed Baghdadi, Mohamed Guenfoud **160**

TULPAR ACADEMIC PUBLISHING

Challenge Journal of Structural Mechanics

A hybrid multi-objective algorithm to predict the characteristics of soil profiles from seismic ground motion records

Zamila Harichane [a,*], Mourad A. Khellafi [b], Amina Sadouki [a]

[a] *Geomaterials Laboratory, Hassiba Benbouali University of Chlef, 02000 Chlef, Algeria*
[b] *Department of Civil Engineering, University of Djelfa, BP 3117 Djelfa, Algeria*

ABSTRACT

The underlying goal of this study is to present an efficient algorithm to identify soil parameters such as thicknesses, shear wave velocities, damping and others parameters of subsurface layers, and site amplification characteristics (natural frequencies, peak amplitudes) from a given pair of seismic records. It is a hybrid procedure combining the stochastic genetic algorithms (GAs) optimization method, to find a point close to the global optimum in the global search phase, and a gradient based local determinist method (Levenberg-Marquardt: LM), to refine the solution. To improve the performance of the global search phase, a multi-objective optimization algorithm is used to minimize the errors between some characteristics of the theoretical amplification function and the experimental one of vertical array records. The weighted sum method which combines the weighted objectives into a single objective function is used to solve the optimization problem. The efficiency of the present algorithm is proven by several examples. Results show that the scheme works well and the curve fitting was always satisfying. Also, the proposed procedure leads to good approximations, requiring a lower computational effort, yet with good rates of convergence. Moreover, neither the growing number of parameters nor the vastness of the search space reduces the efficiency of the algorithm in predicting the characteristics of soil profiles and site amplification commonly required in seismic risk mitigation.

ARTICLE INFO

Article history:
Received 30 June 2017
Revised 27 August 2017
Accepted 13 September 2017

Keywords:
Soil parameter
Amplification function
Genetic algorithm
Seismic record
HMO

1. Introduction

Earthquakes still difficult to be predicted and an important challenge for seismic risk mitigation is thus to develop methodologies to take advantage of ground motion records to extract the information that may help in earthquake hazard reduction. Engineering analysis of strong motion records in previous destructive earthquakes demonstrated that site amplification and associated damage to structures were caused by local site conditions (Ince, 2011; Govindaraju and Bhattacharya, 2012; Tallett-William et al., 2016; Khellafi et al., 2013). Local site amplification, response analysis, and earthquake hazard analysis play one of the most critical roles in seismic studies and geotechnical earthquake engineering (Li, 2014; Guellil et al., 2017). During an earthquake shaking, the bedrock input excitation motion is amplified on the soil surface when propagating in the soil deposit due to natural variability of soil properties. So, the knowledge of the soil properties is essential to understand ground motion modifications due to soil conditions. These soil properties are conventionally obtained by in-situ or laboratory tests which are costly. Alternatively, the inverse analysis can be useful to identify the physical characteristics of a soil medium from the calculated site amplification (Şafak, 1997).

Site amplification is correlated to soil thicknesses, shear wave velocities, material damping and soil densities (Harichane et al., 2005; Kokusho et al., 2005). The identification of site parameters that influence site amplification was studied by several researchers (Rathje and Navidi, 2013; Khellafi et al., 2016).

* *Corresponding author*. Tel.: +213-027-776398 ; Fax: +213-027-721794 ; E-mail address: zharichane@gmail.com (Z. Harichane)
ISSN: 2149-8024 / DOI: https://doi.org/10.20528/cjsmec.2017.09.015

In practice, most natural soil deposits have mechanical properties variables with depth and should be taken into account for reliable dynamic analysis. This goal is reached usually by dividing the soil profile into homogeneous layers, horizontally stratified, with constant properties within each layer, but variable from one layer to another. The SHAKE computer program (SHAKE 2000), for example, incorporates this solution and still widely used by the geotechnical community.

The algorithm given in this paper provide a convenient tool to predict some characteristics of soil profiles and site amplification, more efficiently than an existing one (Harichane et al., 2005, 2012). The soil profiles are idealized as deterministic and/or random multilayered media (Sadouki et al., 2012; Djilali Berkane et al., 2014). Likewise, an approximate manner by assuming an equivalent single layer (Şafak, 1995) may be used to understand site amplification effects. The goal of this study is to present and use a hybrid multi-objective (HMO) algorithm for inverting experimental data to find the best combination of thicknesses of soil layers and their corresponding shear wave velocities and other parameters. The hybrid technique is obtained by combining the stochastic optimization method of Genetic Algorithms (GAs) with the deterministic method of Levenberg-Marquardt (LM). The main interest in using a hybrid technique relies on the fact that, in spite of being a fast technique, the results provided by the LM method strongly depend on the initial guess. For an unsuitable choice of these values the result of the LM method may even diverge (Harichane et al., 2005, 2012). Furthermore, the GAs method usually yields to a relatively large residual error in the identification or to a prohibitively large computational cost. The multi-objective optimization algorithm will provide a set of non-dominant designs where a further improvement for one objective will be at the expense of another. Theses combinations, however, provide results with greater performances, better accuracy and low computational cost, in order to contribute to earthquake risk mitigation by offering a set of some characteristics of soil profiles and site amplification.

2. Identification Procedure

Most of the real world optimization problems are naturally multi-objective; they usually have two or more objective functions which must be satisfied at the same time and possibly are in conflict each other. In order to simplify the solution, many of these multi-objective problems tend to be modeled as mono-objective problems (Deb, 2001). The inverse problem considered here is formulated as a hybrid identification procedure using, firstly, a global multi-objective optimization method via Genetic GAs with only a few iterations to find the best combination of the sought parameters. The optimization problem is formulated as the minimization of the error between: (i) the peaks characteristics (frequencies and amplitudes) of the theoretical amplification functions and the empirical (or measured) ones and, (ii) the shear wave velocity values of the bottom layer and the bedrock. Next, the Levenberg-Marquardt method is used to refine the solutions. This is outlined by the elaboration of a numerical program in FORTRAN language where its algorithm is schematized in Fig. 1.

```
Begin
    INITIALIZE random size population with random individuals
    INITIALIZE probabilities of selection, crossover and mutation
    while no improvement for very long time (2V) do
        EVALUATE individuals, weighting factors and fitness
        SELECT parents randomly from the population
        CROSSOVER parents to obtain offspring
        MUTATE new population
        UPDATE probabilities of selection, crossover and mutation
            if Best fitness improved then
                GROW population size 1
            else if no improvement for long time (V) then
                GROW population size 2
            else
                SHRINK population size
            end if
    end while
        USE best solution as initial guess for LM
    while desired precision is reached do
        EVALUATE Jacobian matrix and increment parameters
        UPDATE parameters
    end while
end
```

Fig. 1. The overall of the proposed procedure.

2.1. Objective functions

The identification of the sought soil properties consists to minimize the differences between model and measured amplification functions. The first objective function is the sum of squared differences between theoretical and empirical curves expressed by the objective function:

$$e_1 = \frac{\sum_{j=1}^{Np} \int_0^{\omega max} |Y_{ei}(\omega) - Y_{di}(\{\gamma\},\omega)|^2 d\omega}{\sum_{j=1}^{Np} \int_0^{\omega max} |Y_{ei}(\omega)|^2 d\omega}, \quad (1)$$

where Y_{di} is the theoretical amplification function given by the model and Y_{ei} is the measured amplification function at the N_P considered points couples. ω_{max} is the maximum circular frequency defining the measured function and $\{\gamma\}$ is the parameters vector to be identified. The second and third objective functions e_2 and e_3, respectively, consist to minimize the differences between the N_k peaks characteristics errors, i.e. the gap between the natural frequencies $\omega_j^{(di)}$ of the theoretical amplification function and the corresponding values of the measured function $\omega_j^{(ei)}$, and the gap between peaks amplitudes $Y_j^{(di)}$ of the theoretical function and the corresponding values of the measured function $Y_j^{(ei)}$, respectively. The fourth (e_4) objective function minimizes the gap between the shear wave velocities at the base of deposit and at the bedrock. These three objective functions are, respectively:

$$e_2 = \sum_{j=1}^{N_k} \left| \omega_j^{e_i} - \omega_j^{d_i} \right|,$$

$$e_3 = \sum_{j=1}^{N_k} \left| Y_j^{e_i} - Y_j^{d_i} \right|,$$

$$e_3 = \left| v_H - v_r \right|. \quad (2)$$

The global objective function is the weighted sum of the preceding expressions:

$$\chi^2(\{\gamma\},\omega) = \sum_{j=1}^{4} w_j e_j, \quad (3)$$

where w_j are the normalized weights and Σw_j=1.

2.2. Levenberg-Marquardt method

The optimization problem expressed in Eq. (3) will be solved by applying a systematic algorithm. To minimize the error function (Eq. 3), its first derivate with respect to each of the unknown parameters has to be calculated as:

$$\frac{\partial \chi_1^2}{\partial \gamma_j} = \frac{\partial (\boldsymbol{X}^T \boldsymbol{X})}{\partial \gamma_j} = 0. \quad (4)$$

The vector $\boldsymbol{X}$ is then expanded into Taylor series and only the first order terms are retained. To improve the convergence of the solution of the resulting system of equations, a damping parameter λ is added to the Levenberg-Marquardt algorithm (Marquardt, 1963). The deterministic Levenberg-Marquardt (LM) method consists in constructing an iterative procedure which starts with an initial guess $\boldsymbol{A}^0$ and at the $(k+1)^{th}$ iteration, the new estimate is given by:

$$\{\gamma\}^{k+1} = \{\gamma\}^k + \Delta\{\gamma\}^k, \quad k = 0,1,2,\ldots, \quad (5)$$

with the variation $\boldsymbol{\Delta}\{\gamma\}^k$ being computed from:

$$\Delta\{\gamma\}^k = -[(J^T)^k J^k + \lambda^k I]^{-1} (J^T)^k X^k, \quad (6)$$

where **I** is the identity matrix and **J** the Jacobian matrix.

The iterative procedure is continued until some convergence criterion is satisfied. Being deterministic and based on the Jacobian matrix that depends on the gradients, the LM method presents a fast convergence but with the risk to stop in a relative minimum. Furthermore, as mentioned before, if the initial guess is a reasonable one (as the one obtained by the GAs method) then the LM is likely to achieve the desired minimum with few iterations (Walter and Pronzato, 1997).

As this paper deals with an inverse analysis to identify the sought parameters by using down-hole array records, the acceleration recorded at the bedrock and at the ground surface are needed to calculate the objective function for the optimization problem. Fourier amplitude spectra between recorded and calculated accelerations will be smoothed such that the error functions converge.

2.3. Genetic algorithms method

Since there is several number of extrema in the error function due to the use of seismic data, it seems to be not effective to apply a gradient method. Then GAs may be effective in such problem (Goldberg, 1989). Unlike traditional methods, a GA searches a global optimal solution and does not need to calculate the gradient of the objective function and thereby makes GA a highly promising tool (Kao et al., 2010; Pezeshk and Zarrabi, 2005; Koh and Perry, 2007; Sato et al., 2013). The GA is well suited to solve large combinational design problems.

The creation of the initial population is a blind random search for the solution in the large space of possible solutions. GAs are powerful tools for locating an optimal model by rapidly exploring model space. They make use of a stochastic search through model space employing a transition probability rule to improve the solution (Rodríguez-Zúñiga et al., 1997). Then, once a population of models (i.e. parent) is created, the GA scheme evaluates and selects individuals for reproduction, generates new individuals by mutation, crossovers, and direct reproduction, and finally creates new generation in all iterations (Koza, 1992).

3. Measured and Model Functions

3.1. Measured functions

In the present study two measured function are used. The first one is the standard spectral ratio technique (SSR) which computes the ratio of the Fourier transform of the signal at the measuring point to the same quantity at the reference point as:

$$Y_{ei}^{(sr)}(f) = \frac{F_s(f)}{F_{sr}(f)}, \quad (7)$$

where f is the frequency, $F_s(f)$ and $F_{sr}(f)$ are the Fourier transforms (F) of the ground surface and the reference rock records (generally the acceleration data), respectively. A smoothing technique is used to reduce the effects of noise which is always present in the records.

An alternative to spectral ratios, is the cross spectral ratio (CSR) (Şafak, 1997). This technique computes the amplification (measured) function as the ratio:

$$Y_{ei}^{(cs)}(f) = \frac{F_{rs}(f)}{F_{rr}(f)}, \tag{8}$$

where $S_{rr}(f)$ is the power spectral density of the reference rock record, and $S_{rs}(f)$ is the cross-power-spectral density between the reference rock and the ground surface records (Fig. 2).

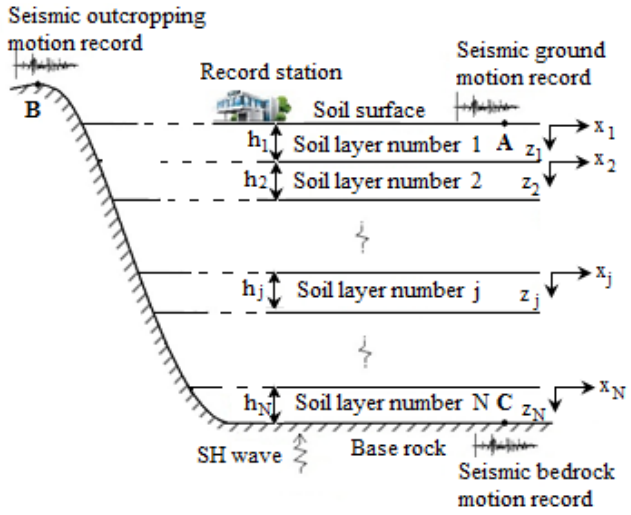

Fig. 2. Ground response nomenclature of a soil deposit overlying bedrock.

3.2. Model functions

Several theoretical models related to the 1-D SH wave propagation in a linear viscoelastic soil deposit to model the soil behavior during earthquakes exist. Some of these model functions needed to achieve the identification procedure are used in the present study.

3.2.1. Amplification function of an equivalent single layer over bedrock

This model was proposed by Şafak (1995). It harmonizes the amplification function with that of an equivalent single homogeneous layer over bedrock as:

$$Y_{di}^{(es)}(f) = \frac{(1+r)^{-\pi f\tau/Q}}{\left[1+2r\cos(4\pi f\tau)e^{-2\pi f\tau/Q}+r^2e^{-4\pi f\tau/Q}\right]^{1/2}}. \tag{9}$$

In Eq. (9), r represents the reflection coefficient at the interface between the soil layer and the bedrock for the up-going waves. τ is the one-way travel time of waves in the layer and Q, which is called a quality factor, represents the damping in the soil. The unknown parameters governing this model are r, τ, and Q and will be identified using a given pair of soil- and rock-site records in conjunction with the identification procedure, in frequency domain.

3.2.2. Amplification function of a multilayers soil deposit

This function was widely used to study site amplification and site response according to the 1-D SH waves propagating in homogeneous as well as inhomogeneous layered deposits (Wolf, 1985; Harichane et al., 2005; Sadouki et al., 2012; Khellafi et al., 2016; Guellil et al., 2017). The soil medium is idealized as a layered soil deposit consisting of N horizontal homogeneous isotropic viscoelastic layers (Fig. 2) overlying a bedrock. More details on the evaluation of this amplification function may be found in the cited references and in the Appendix A.

3.2.3. Normalized cross spectral density function of random media

This model matches, in a simple stochastic manner; the inherent variability of soil properties. Djilali Berkane et al. (2014) used this model to investigate the contribution of soil layers stochasticity in spatial variation of seismic response spectra. They obtained free response spectra by random vibration theory starting from the cross spectral density of the total ground surface displacement due to incident random waves impinging the bedrock layer, given by Zerva and Harrada (1997). The normalized cross spectral density function of the random media is given by:

$$S(\omega) = [\omega_0^4 + (2\beta + 4\xi_0^4 - 2)\omega_0^2\omega^2 + (\beta-1)^2\omega^4]\cdot |T^{dl}(\omega)|^2 + 4\beta^2\omega_0^4\omega^2\sigma_{\omega\omega}^2\cdot|T^{dl}(\omega)|^4, \tag{10}$$

where β is the participant factor, ω_0 the natural frequency, ξ_0 the damping ratio and $\sigma_{\omega\omega}$ the standard deviation of the natural frequency of the random media. $T^{dl}(\omega)$ is the harmonic amplification function of a single degree of freedom oscillator with frequency ω_0 and damping ξ_0:

$$|T^{dl}(f)|^2 = \frac{1+4\xi_0^2(f/f_0)^2}{\left[1-(f/f_0)^2\right]^2+4\xi_0^2(f/f_0)^2}. \tag{11}$$

4. Results and Discussions

4.1. Comparison between measured and model functions

Before using the inverse analysis, the efficiency of the model functions to match the measured ones is studied by comparing different measured amplification functions (MAFs) and theoretical ones (TAFs) with experimental data recorded within the Garner Valley Downhole Array (GVDA) using actual surface to depth input data. The Garner Valley (California) downhole array was performed to improve the understanding of the effects of

a shallow soil site on ground motion. The characteristics of the soil profile of the Garner Valley site upper the 22 *m* are given in Refs (Pecker and Mohammadioun, 1991; Steidl et al., 1996). A small-magnitude (M_L=2.5) motion recorded from a large collected motions during the period 1989-1991 was selected for computational purposes. Recorded accelerograms (horizontal components) obtained at this site are the same used by (Harichane et al., 2005). All empirical techniques use 4096 points FFT (Fast Fourier Transform) and corresponding curves are smoothed by using a triangular window of 0.5 Hz width.

The TAF is computed according to Harichane et al. (2005) using the properties given in Refs (Pecker and Mohammadioun, 1991; Steidl et al., 1996). The resulting plots of amplification functions for frequencies interval between 0 and 20 Hz are presented in Fig. 3. For clarity, Table 1 summarizes the natural frequencies (*f*) and the corresponding peak amplitudes (*PA*) that characterize the different functions. Examination of Fig. 3 shows a good agreement in terms of natural frequencies. However, it can be seen that the TAFs amplitudes are greater than the MAFs ones due the low damping values (1-4%). Also, the SSR technique gives greater amplification than the CSR but still lower than theoretical ones; though the natural frequencies (obtained with any technique) are generally in concordance.

Therefore, the identification procedure of soil parameters using curve fitting between any MAFs and TAFs methods is possible. In order to ensure a sufficient accuracy and reduce the computational cost when using the GAs method, the normalized weights in Eq. (3) should be chosen so that the global objective function is minimized by focusing the weight (w_2) of the natural frequencies error (e_2) and penalizing the weight (w_3) of the amplitude peak errors (e_3). We should also not take into account the gap error between peak amplitudes associated with the fundamental frequency in the calculation of the error e_3 because of the large deviations observed between MAFs and TAFs peak amplitudes at this frequency.

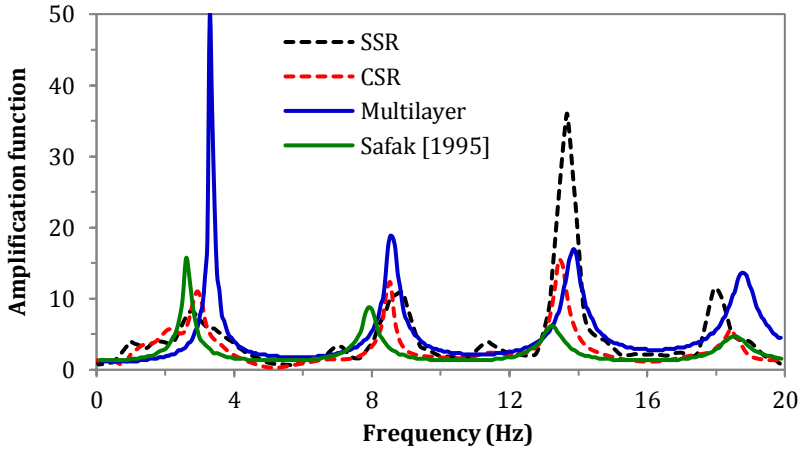

Fig. 3. Comparison of different MAFs and TAFs between free surface and 22 m depth at GVDA site.

Table 1. Comparison of natural frequencies and corresponding peak amplitudes (PA) of different MAFs and TAFs between free surface and 22 m depth at GVDA site.

Mode	1		2		3		4	
Frequency /Peak Amp	*f* (Hz)	PA	*f* (Hz)	PA	*f* (Hz)	PA	*f* (Hz)	PA
SSR	2.8	8.3	8.9	11.0	13.7	36.0	18.0	11.5
CSR	3.1	11.0	8.7	12.2	13.5	15.3	18.3	5.9
Multilayer formulae	3.4	49.9	8.6	19.5	13.9	16.6	18.8	13.7
Şafak (1995) formulae	2.7	15.6	8.7	8.7	13.3	6.0	18.6	4.5

4.2. Identification of soil profiles characteristics

The effectiveness of the proposed algorithm is illustrated through several examples where its stability in adapting itself to match a given target is shown. In the first example, the present algorithm is applied to identify the parameters of an equivalent single layer corresponding to the best match of the theoretical and measured amplification functions with the GVDA site data. In the other cases, the validity of the present scheme is demonstrated with numerical applications.

4.2.1. Identification of characteristics of an equivalent single layer

As defined by Eq. (9), the design variables for this problem consist of three unknowns which are *r*, *Q* and τ. Their identification is performed on the search space including all possible values: 0-1 for *r*, 0-1*s* for τ and 1-100 for *Q*. The soil amplification function between free surface and 22 m depth is computed by the SSR and the CSR methods. The procedure has been tested for effectiveness for the GA method with several population sizes,

number of maximum generations, probability of crossover and mutation. With both methods (GA and LM), the objective functions used are given by Eq. (3). The normalized weights to be considered with the GA method will be determined to obtain the best results according to the considered models. Since the Şafak (1995) model does not permit to calculate the shear wave velocity at the base of the layer, the normalized weight $w_4 = 0$; therefore only two parameters, w_1 and w_2 are used because the third one is $w_3 = 1 - w_1 - w_2$. For these cases, a graphical shape of the objective function (Fig. 4) is established. Thereby the smoothness properties of the surface can be examined as well as the location of the optimum solution. Only two optimization parameters are involved, which means that the objective function surface is illustrated in a three dimensional space. It is obviously very difficult to inspect the function graphically if more than two optimization parameters are required.

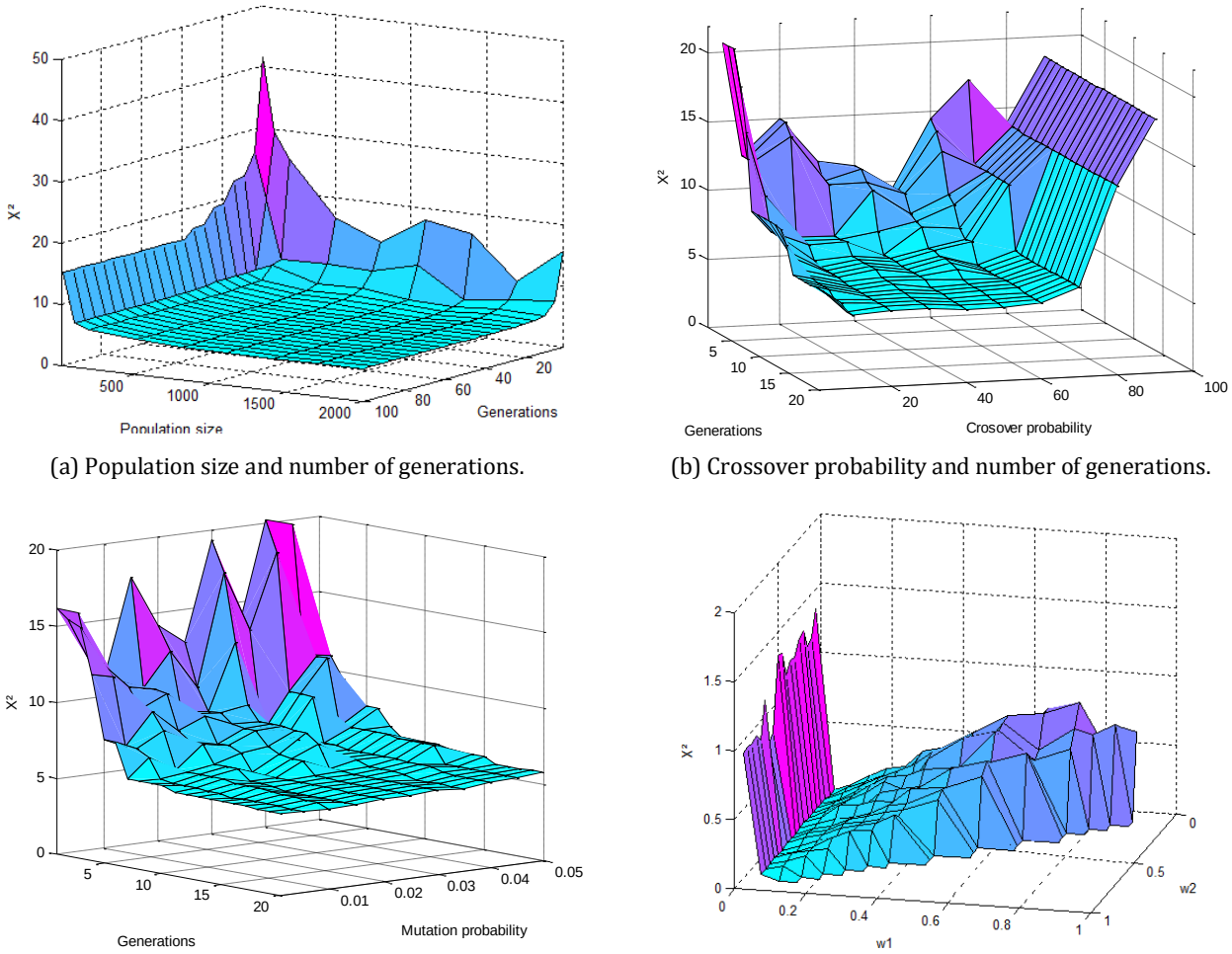

(a) Population size and number of generations.

(b) Crossover probability and number of generations.

(c) Mutation probability and number of generations.

(d) Objective function space versus w_1 and w_2.

Fig. 4. Convergence history of the GA method versus.

The obtained results indicate that simultaneous increases of the population size from 20 to 2000 and the number of maximum generations from 5 to 100 have considerably improved the performance of the algorithm (Fig. 4a). A population size of 800 founds the solution in 58 GA generations and 7 LM iterations, while a population size of 1400 founds the solution in only 16 GA generations and 5 LM iterations. The crossover operation was sensitive in perturbing the objective space (Fig. 4b). As the crossover increased from 20% to 60%, the solution was found in only 16 generations. But, when the crossover rate was outside this interval, the objective function moved away from the minimum values. Consequently, the closest solution corresponding to a crossover value of 40% was chosen for the optimization process. The mutation operation was not as sensitive in perturbing the objective space when the number of generations is greater than 16. So, there was no particular difference observed when the mutation operator is increased from 0.1% to 5% (Fig. 4c). Nevertheless, a value of 0.1% provides the best solution as compared to the others. However, when the number of generations decreases below 14, the objective function increases in a remarkable way with the decrease of the generations number. The normalized weights are sensitive in perturbing the objective space (Fig. 4d). The results show that variations are more pronounced with respect to parameter w_1 with minimums values observed at w_1 = 5%, and are fairly constant with respect to the parameter w_2. The corresponding weights which led to the best result are: w_2 = 60% and w_3 = 35%. Table 2 summarizes the optimal values for the GA parameters that were used for

the optimization. During the first generation of the GA, the variables of the population were initiated randomly. While, for the further generations the variables were modified using the genetic operators of crossover and mutation. At the end, a few numbers of iterations with LM (2 to 9) was sufficient to refine the solutions. It is noticed that results can be improved mainly by increasing the population size or the number of generations. Generally, the optimization process works satisfactorily and led towards an optimal solution.

Table 2. Optimal parameters chosen for GA from sensitivity analysis.

Parameter	Population size	Number of generations	Crossover probability (%)	Mutation probability (%)	Normalized weights (%)			
					w_1	w_2	w_3	w_4
Optimal value	1400	20	40	0.1	5	60	35	0

Fig. 5 shows the evolution of populations for successive generations during the GA optimization phase for the identification of the parameters of the model. The associated evolution of the objective function versus the population generation number is plotted in Fig. 6. This figure shows that the optimization procedure permits to obtain approximate solutions within a margin of error of 10% after 16 generations only. The identification results are compared in Table 3 with actual ones. A good agreement is observed between actual and identified values of r and τ. Nevertheless, the identified values of Q are slightly different from the actual ones within a margin of error of 20%.

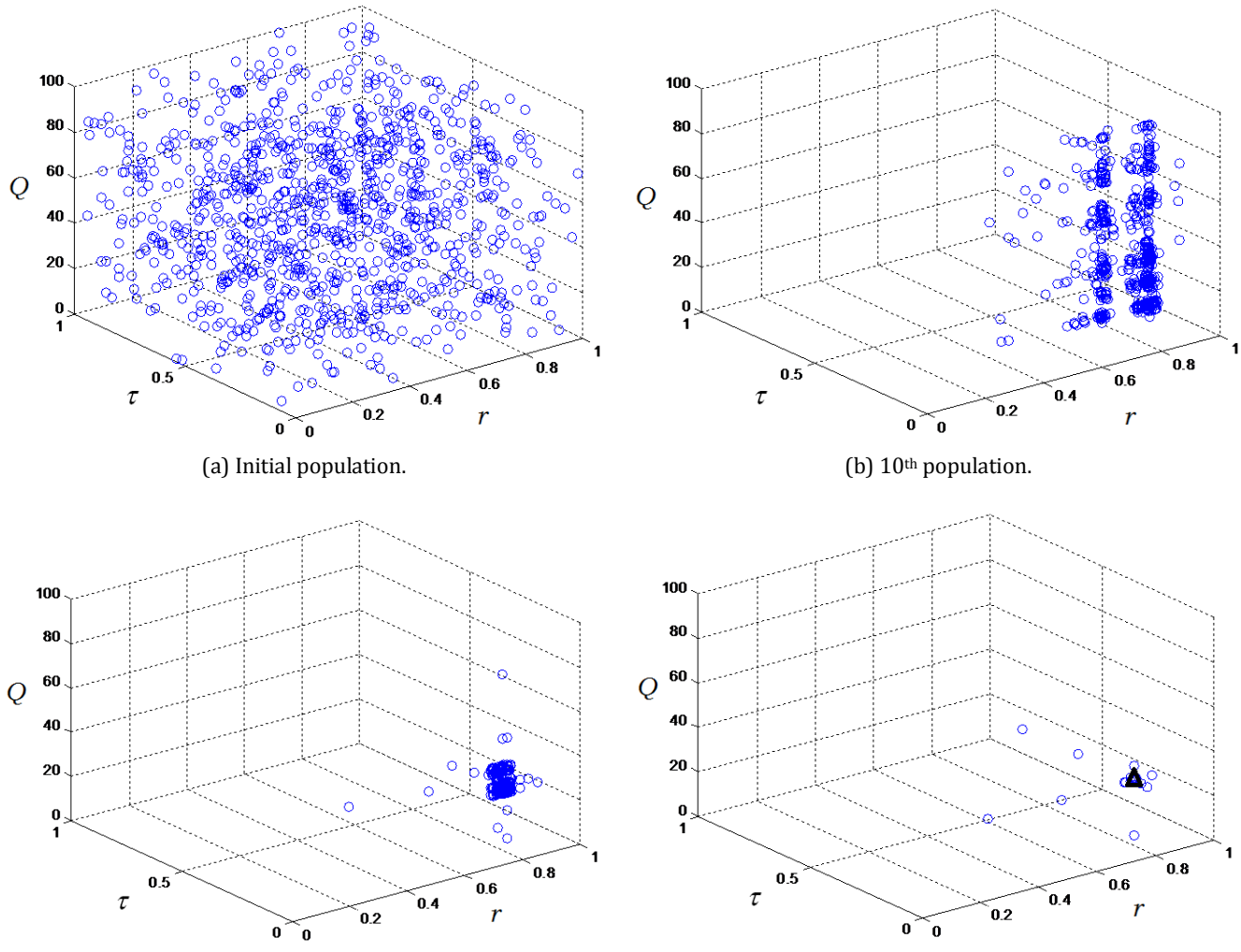

(a) Initial population. (b) 10th population.

(c) 17th population. (d) 30th population.

Fig. 5. Evolution of population in the GA method for the identification of parameters r, Q and τ. Points denoted **o** are individuals in the search space; point denoted **Δ** is the final solution.

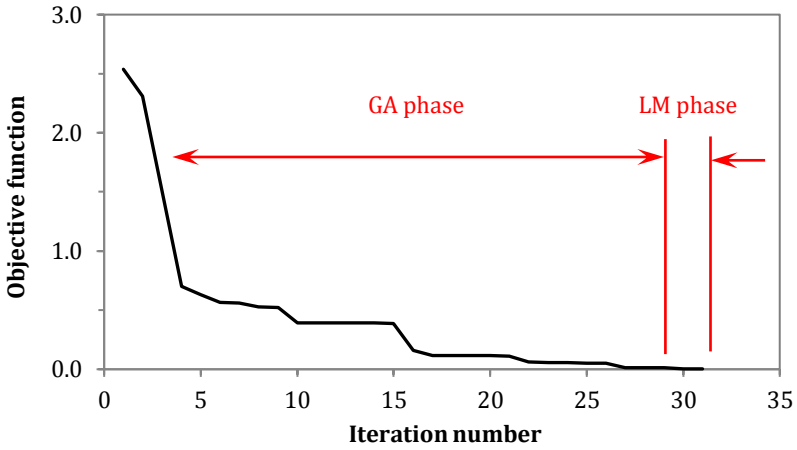

Fig. 6. Evolutions of the objective function versus iteration number.

Table 3. Comparison between identified and actual parameters values for equivalent single layer at the GVDA site.

Actual values		Identification with SSR		Identification with CSR	
		Mono-objective optimization	Multi-objective optimization	Mono-objective optimization	Multi-objective optimization
r	0.8	1.0	0.9	0.8	0.9
τ	0.1	0.01	0.1	0.1	0.1
Q	32.4	65.7	37.5	40.0	39.1
Objective function		0.2	0.5	0.3	0.4

To show the effectiveness of the proposed algorithm, the identification results for, firstly, a hybrid mono-objective (H-Momo-O) optimization method and, secondly, with a hybrid multi-objective (H-Multi-O) one are compared in Fig. 7 and Table 3. Fig. 7a shows that the H-Mono-O procedure has been unsatisfactory. Even after several trials with more population sizes and generations it was not possible to closely approach the optimal solution although the error with the one objective function is less than that given by the H-Multi-O.

These results mean that during the optimization process, the GAs method searches the minimum error without taking into account the amplification function shapes. With this approach, the obtained error is less than that brought by the H-Multi-O but the curve fitting is bad; which is the advantage brought by the H-Multi-O method to the identification process. With this method, the optimization is guided by an objective function which takes into account the shape of the amplification function by minimizing in addition, the gap between the resonance frequencies and the corresponding amplitudes. Fig. 7b shows that the H-Mono-O identification is better compared to the previous case, but remains less than the H-Multi-O identification. This is due to two factors: the first one is that the CSR amplification function gives peaks amplitudes smaller than those obtained with the SSR method and do not change abruptly with frequency like with the third resonant peak. The second one is that the function identified with the H-Mono-O agrees better with the shape of the amplification function. Consequently, the H-Multi-O identification seems to work best to cover imperfections that may be encountered with the amplification function shapes.

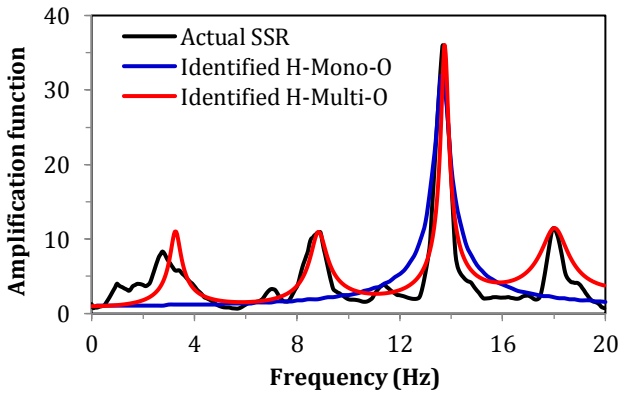

(a) Identification using the SSR method.

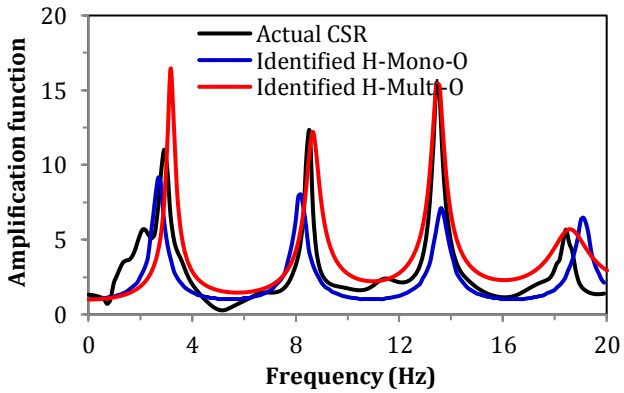

(b) Identification using the CSR method.

Fig. 7. Comparison between empirical and identified amplification functions at GVDA site.

4.2.2. Identification of characteristics of a multilayers soil profile

This application consists in the validation of the present algorithm with a numerical example. It consists to identify properties values of an actual nuclear power plant site as specified in Table 4.The parameters identification is assumed to be performed on a search space including all possible values: 0-50 m for h, 1000-2500 kg/m^3 for ρ, 100-1500 m/s for v_s, 0-10% for ξ. The parameters of the GA optimization are the same as in the precedent example.

Table 4. Characteristics of an actual site of a nuclear power plant (Wolf, 1985).

Depth (m)	Shear wave velocity (m/s)	Mass density (kg/m^3)	Damping ratio (%)
0 – 5	200	2000	7
5 – 10	250	2000	6
10 – 20	350	2000	5
20 – 30	500	2200	5
30 – 40	800	2200	5
40 – 50	1000	2400	4
(bedrock)	1500	2500	2

a) Identification of all parameters

As was done previously, to evaluate the representativeness of the identified solution, different optimizations are performed in the same search space. The only difference concerns the initial GA population that is each time randomly selected in the search space. Results show that the solution to this problem is not unique. The identification process leads then to a very large range of possible values for each parameter. However, the proposed procedure works well and the curve fit is very good, but with very high computational cost. When the layers number N is considered unknown, the number of the sought parameters is variable and equal to $4N+1$. The identification is done in several successive steps, where within each step the procedure is run with the value of N being constant and varies from 1 to 10. The path from one step (n) to the next (n+1) is controlled by a transition condition which minimizes the difference between the average shear wave velocities of the n^{th} layer already identified and of the $(n+1)^{th}$ layer to be identified of the soil deposit:

$$e_5 = |\bar{V}_s^{n+1} - \bar{V}_s^n| \quad , \quad \bar{V}_s^n = \frac{\Sigma_{j=1}^n h_j}{\Sigma_{j=1}^n \frac{h_j}{v_{sj}}} \quad . \tag{12}$$

In this case, a very good curve fit from five layers soil profile is obtained. Fig. 8 shows the obtained minimum error function versus the number of layers. It should be noted that the curve fitting is very good for 3 layers as well as for 6 layers soil profiles. It can be deduced from these tests that the solution is not unique. Nonetheless, despite the vastness of the search space when the number of sought parameters is important it is not needed to highly increase the population size or the number of GA generations of the optimization methods in order to reach the objective. In spite of that, the proposed hybrid multi-objective algorithm is still working fine regardless the difficulties met in this kind of optimization problems.

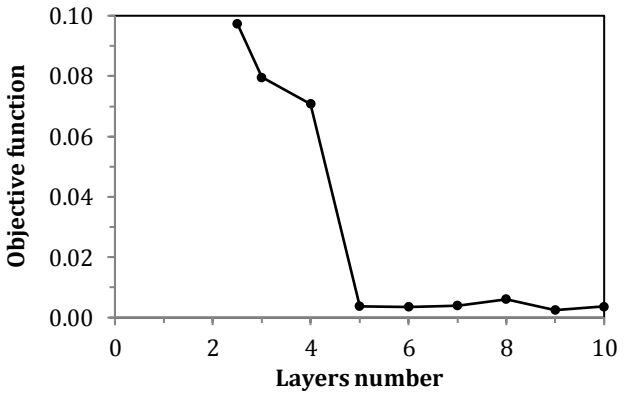

Fig. 8. Minimum objective function versus layer number.

b) Identification of reduced number of parameters

In the identification process, the GA parameters and the search space are the same as in the precedent case and the layers number is considered known (N=6). First, the process is repeated for the identification of one parameter per layer, then, the process is repeated for the identifications of two parameters per layer and finally three parameters per layer.

For the first case, the number of identified parameters is equal to 6. The proposed procedure has been accomplished successfully for the identification of h_j, v_{sj} and ξ_j, separately. The values of these parameters were identified exactly with a very good agreement between the identified and the actual curves (Fig. 9). However, the procedure has failed to identify exactly the values of ρ_j. This is because mass densities for two successive layers are dependent in the expression of q_j (Appendix A) and should not be explored independently. For the second case, the number of identified parameters is equal to 12. Herein, the proposed procedure has identified exactly the values of h_j, v_{sj} and ξ_j except in the case where h_j and v_{sj} were identified together. In this last case, h_j and v_{sj} are dependent in the ratios h_j/v_{sj} and v_{sj}/v_{sj+1} that prevents their identification (in expression Λ in Eq. (A.3) in the Appendix A).

For the third case, the number of identified parameters is equal to 18. The identification has been disappointing and it was not possible to closely approach the known solution. Different solutions consisting of different combinations of the sought parameters were obtained by running the proposed inversion process that resulted in a very good agreement between the identified and the actual curves (Fig. 9).

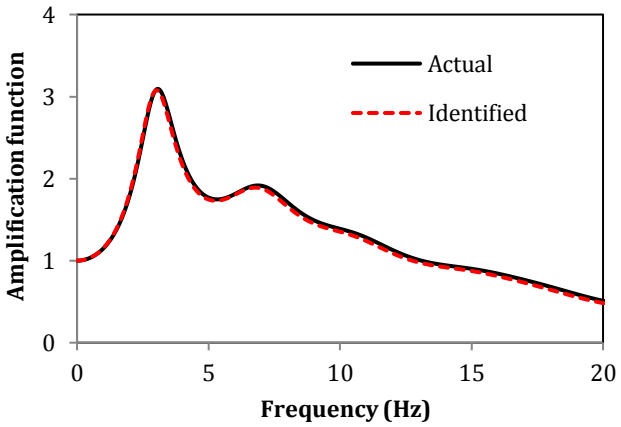

Fig. 9. Comparison between actual and identified amplification functions for a nuclear power plant.

Consequently, the proposed procedure has failed to well identify the parameters of a multilayers soil deposit especially when the number of unknown parameters is larger than three parameters per layer. Analysis of results has shown that the parameters are dependent each other and cannot be identified independently, which explains the existence of different solutions. The expansion of the search space has not decreased the performances of the proposed procedure. Indeed, the process converges constantly to a final solution without increasing the population size or the number of generations.

4.2.3. Identification of characteristics of a randomly inhomogeneous layer via the normalized cross spectral density

This application is dedicated to identify the parameter ξ_0, ω_0, β and $\sigma_{\omega\omega}$ of a random inhomogeneous layer modelling a soil deposit as defined by Eq. (10). The minimization is done by using the normalized cross spectral density function. The identification procedure is performed on the following search space: 0-100 rad/s for ω_0, 0-10% for ξ_0, 0-10 for $\sigma_{\omega\omega}$, 0-10 for β. The actual characteristics of the random layer are specified in Table 5 (Djilali Berkane et al., 2014) and the parameters of the GA optimization are the same as in the first example.

Table 5. Comparison between actual and identified parameter values of a randomly inhomogeneous layer via the normalized cross spectral density.

Parameters	Actual values	Hybrid multi-objective procedure	
		GA only	Final
ω_0 (rad/s)	3.05	3.16	3.05
ξ_0 (%)	5.0	6.0	5.0
$\sigma_{\omega\omega}$	0.12	0.01	0.12
β	1.0	0.5	1.0

Initially, the identification has been very disappointing and it was not possible to closely approach neither the known solutions nor the actual curve with sufficient accuracy. To improve the identification accuracy and efficiency, therefore, we have conducted several tests by changing the parameters of the above optimization. Analysis shows that efficiency increases significantly with higher values of normalized weight w_1 without modifying as much the GA's parameters. The normalized weights that provide the required solutions with low computational cost are: $w_1 = 80\%$ $w_2 = 10\%$ $w_3 = 10\%$ $w_4 = 0\%$.

An important number of iterations with LM (25 to 45) are needed to refine the solutions. Fig. 10 shows an example of the curve fitted to the actual one.

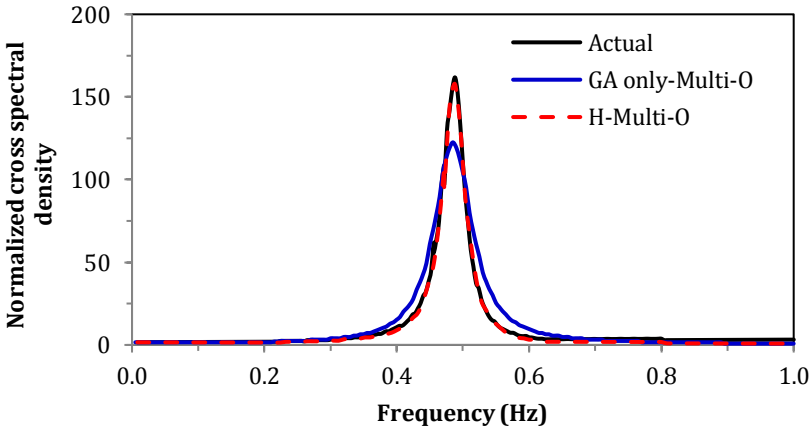

Fig. 10. Comparison between actual and identified normalized cross spectral densities for a nuclear power plant.

To explain these changes, the topology of the objective function is plotted versus two optimization variables (Fig. 11) as if more than two optimization variables are required it is obviously very difficult to inspect the function graphically.

In Fig. 11a, it can be seen that the objective function surface has a unique and well-defined minimum but in very small space close to this minimum. Thus, by comparing this space to the predefined search space, it is clear that the identification is not easy. Moreover, it can be observed in Fig. 11b that the objective function surface describes a flat and long valley in the search space in which the minimum is not well defined. Though, it is known that the narrowness of the valley greatly decreases the probability of finding the solution with evolutionary programming algorithm (Dunning, 1998), which explains the necessity of a large number of gradient iterations to reach the local minimum.

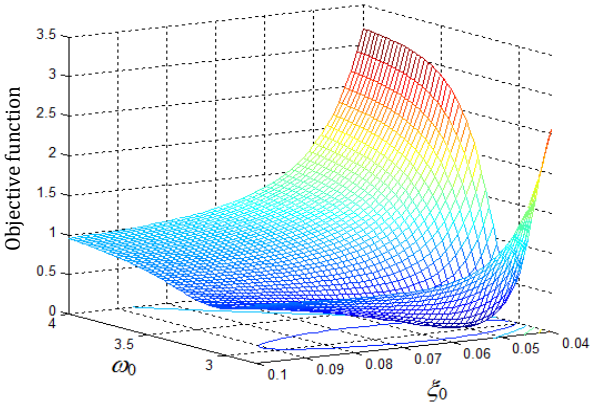

(a) The objective function versus ω_0 and ξ_0.

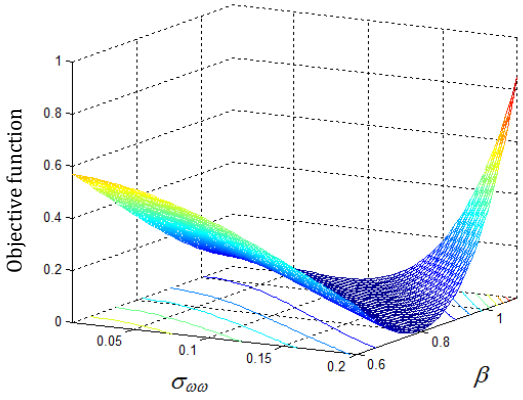

(b) The objective function versus β and $\sigma_{\omega\omega}$.

Fig. 11. Topology of the objective function close to the sought minimum.

Furthermore, when increasing the number of generations in the GA optimization, a few numbers of gradient iterations is needed to refine the solutions. For example, with 50 generations in the GA optimization, 4 to 9 of LM iterations are sufficient to achieve the planed goal (Fig. 12). But increasing the population size in the GA optimization does not give improvement.

5. Conclusions

The present study concerned the identification of soil profile characteristics such as layer's thicknesses, shear wave velocity, mass density, damping, and some site amplification characteristics (natural frequencies, peak amplitudes) from a pair of records of priori known of soil constitutive equation from typical earthquake records by inverse analysis. These inverse problems are solved by minimizing the errors between the theoretical and empirical amplification functions of the subsurface layers of vertical array records. A hybrid multi-objective (HMO) optimization algorithm combining the genetic algorithms (GAs) and the traditional based gradient method (LM) is presented. Several examples were carried out in order to test the efficiency of the algorithm.

The gradient method seems to be robust and efficient only if the shape of the objective function is relatively smooth or if the initial guess is very close to the solution. While the genetic algorithm enables the convergence of a set of solutions close to the best one even with a flat or noisy error function. In order to ensure convergence of the genetic algorithm method with low calculation cost, the population is guided towards the preferred solutions with four objective functions. It is shown that the (HMO) method GA-LM leads to good approximations for the global minimum, requiring a lower computational effort, yet with good rates of convergence. Nevertheless, the normalized weights should be chosen so that the global objective function is minimized by focusing the weight of the natural frequencies error and penalizing the weight of the amplitude peaks errors, and do not take into account the gap error between peak amplitudes associated with the fundamental frequency in the calculation of the objective function.

The hybrid identification scheme is validated by using experimental data recorded within the Garner Valley Downhole Array (GVDA) and numerical applications for the other cases. The identified amplification function is best fitted with the CSR than with the SSR curves.

Nevertheless, despite the observed differences in the SSR and CSR peak amplitudes, a good agreement was observed between actual and identified parameters within a margin of error of 20%. Moreover, this algorithm seems to be very efficient as long as the optimization is guided by an objective function which takes into account the form of the amplification function. For numerical examples, results show that the present algorithm works well and the curve fit was always very good. However, neither the growing number of parameters nor the vastness of the search space tends to reduce the efficiency or the robustness of the present algorithm. Nevertheless, exact identification of parameters of different models is possible only if these parameters are independents. So, if some parameters are known, the remainder can be identified exactly.

This proposed algorithm is very operative in estimating the characteristics of soil profiles and site amplification required in earthquake hazard analyses, with a

much reduced cost compared to the laboratory or in-situ conventional methods, taking advantage of existing seismic ground motion records. It may be easily extended to extract soil parameters of two soil profiles from only free field acceleration records. On the other hand, to be efficiently applied to strong ground motions, an adequate model function in the framework of nonlinear analysis has to be used.

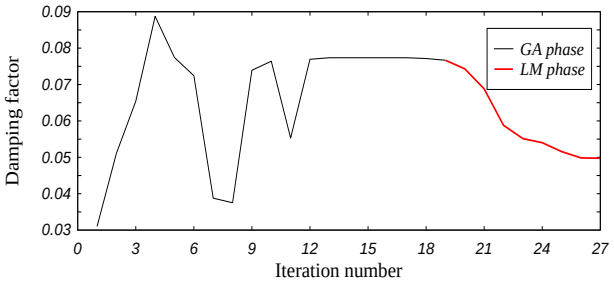

(a) Convergence history of the identified damping factor.

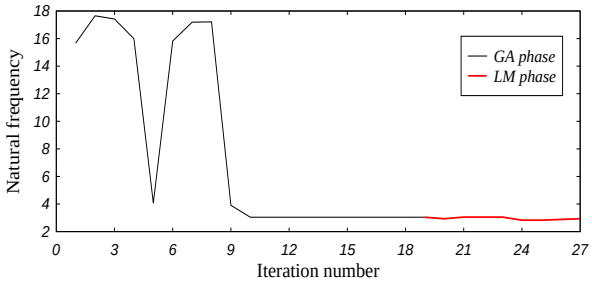

(b) Convergence history of the identified natural frequency.

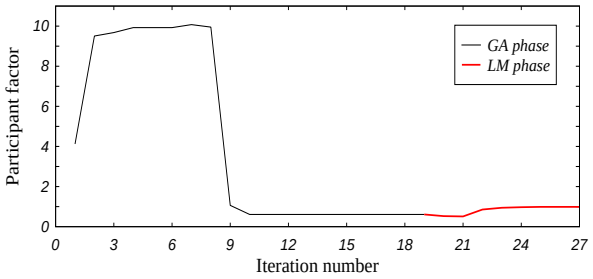

(c) Convergence history of the identified participant factor.

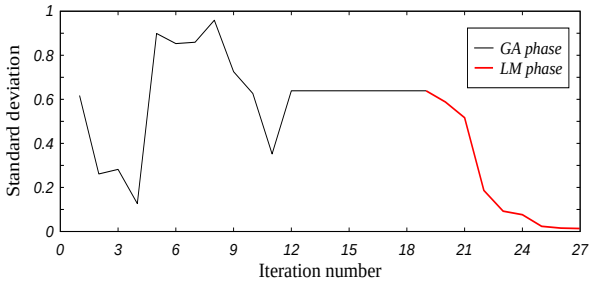

(d) Convergence history of the identified standard deviation.

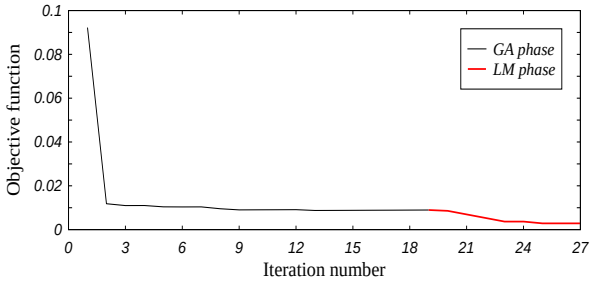

(e) Convergence history of objective function.

Fig. 12. Convergence history of the optimized parameters.

Appendix A.

The TAFs for a harmonic motion with frequency, $\omega=2\pi f$, are given by (Harichane et al., 2005).

$$T_1^{hm}(\omega) = \frac{2^{N+1}}{\sum \Lambda_{ml}} \qquad m, l = 1,2\,, \tag{A.1}$$

and

$$T_2^{hm}(\omega) = \frac{2^{N}}{\sum \Lambda_{1m}} \qquad m = 1,2\,, \tag{A.2}$$

where $T_1^{hm}(\omega)$ and $T_2^{hm}(\omega)$ are, respectively, the theoretical soil-to-bedrock and soil-to-rock outcropping TAFs, respectively, and Λ_{ml} are the components of the 2×2 matrix $\mathbf{\Lambda}$ which is:

$$\Lambda = \prod_{j=N}^{1} \begin{bmatrix} (1+q_j)e^{ik_j h_j} & (1-q_j)e^{-ik_j h_j} \\ (1-q_j)e^{ik_j h_j} & (1+q_j)e^{-ik_j h_j} \end{bmatrix}, \tag{A.3}$$

where $k_j = \omega / v_{Sj}$ is the wave number and

$$q_j = \rho_j v_{Sj} / \rho_{j+1} v_{Sj+1}\,. \tag{A.4}$$

The impedance ratio at the interface between layers j and j+1, v_{Sj} ($v_{Sj} = \sqrt{G_j/\rho_j}$) is the shear wave velocity, h_j is the layer thickness and i ($i^2 = -1$) the complex number. For a damped case, the formally treated equations still hold, by replacing shear modulus G_j by $G_j\left(1 + 2i\xi_j\right)$.

The soil properties (shear modulus G_j, mass density ρ_j and damping ratio ξ_j) are constants within each layer j but different among layers.

REFERENCES

Deb K (2001). Multi-Objective Optimization Using Evolutionary Algorithms. John Wiley & Sons, Inc. New York, NY, USA.

Djilali Berkane H, Khellafi MA, Harichane Z, Kouici W (2014). Stochastic study of the spatial variation of ground response spectrum. *Electronic Journal of Geotechnical Engineering*, 19, 4345-4361.

Dunning T (1998). Recorded Step Directional Mutation for Faster Convergence. In Evolutionary Programming VII. Springer Berlin Heidelberg, Germany.

Guellil ME, Harichane Z, Djilali Berkane H, Sadouki A (2017). Soil and structure uncertainty effects on the soil-foundation-structure dynamic response. *Earthquakes and Structures*, 12(2), 153-163.

Goldberg DE (1989). Genetic Algorithms in Search, Optimization and Machine Learning. Addison-Wesley Longman Publishing Co., Inc. Boston, MA, USA.

Govindaraju L, Bhattacharya S (2012). Site-specific earthquake response study for hazard assessment in Kolkata city, India. *Natural Hazards,* 61(3), 943–965.

Harichane Z, Afra H, Elachachi SM (2005). An identification procedure of soil profile characteristics from two free field accelerometer records. *Soil Dynamics and Earthquake Engineering*, 25(6), 431-438.

Harichane Z, Afra H, Bahar R (2012). Experimental validation of an identification procedure of soil profile characteristics from free field acceleration records, *International Journal of Geotechnical Earthquake Engineering*, 3(1), 1-17.

Ince GC (2011). The relationship between the performance of soil conditions and damage following an earthquake: a case study in Istanbul, Turkey. *Natural Hazards and Earth System Sciences,* 11(6), 1745-1758.

Jones AL, Kramer SL, Arduino P (2002). Estimation of uncertainty in geotechnical properties for performance-based earthquake engineering. PEER Report 16, Pacific Earthquake Engineering Research Center, University of California, Berkeley, USA.

Kao CY, Chung JK, Yeh YT (2010). A comparative study of the least squares method and the genetic algorithm in deducing peak ground acceleration attenuation relationships. *Terrestrial, Atmospheric and Oceanic Sciences*, 21(6), 869-878.

Khellafi MA, Harichane Z, Hamid A, Sadouki A (2013). A case study of accelerometric records analysis of May 21st, 2003, Boumerdes (Algeria) Earthquake. *International Journal of Geotechnical Earthquake Engineering,* 4(2), 34-52.

Khellafi MA, Harichane Z, Hamid A, Erken A (2016). Prediction of parameters of soil stratums and earthen dams from free field acceleration records. *International Journal of Geotechnical Earthquake Engineering,* 7(1), 33-56.

Koh CG, Perry MJ (2007). Structural damage quantification by system identification. *Journal of Earthquake and Tsunami*, 1(3), 211-231.

Kokusho T, Aoyagi T, Wakynam A (2005). In situ soil-specific nonlinear properties back-calculated from vertically array records during 1995 Kobe earthquake. *Journal of Geotechnical and Geoenvironmental Engineering,* 131(12), 1509-1521.

Koza JR (1992). Genetic Programming, On the Programming of Computers by Means of Natural Selection, MIT Press, Cambridge, MA, USA.

Li Z (2014). Uncertainty of soil properties in earthquake ground-motion site response analyses. Tenth U.S. National Conference on Earthquake Engineering Frontiers of Earthquake Engineering, Anchorage, Alaska, USA, July.

Marquardt DW (1963). An algorithm for least-squares estimation of nonlinear parameters. *Journal of the Society for Industrial and Applied Mathematics*, 11, 431-441.

Mercado V, El-Sekelly W, Zeghal M, Abdoun T (2015). Identification of soil dynamic properties through an optimization analysis. *Computers and Geoterchnics*, 65, 175–186

Pecker A, Mohammadioun B (1991). Downhole instrumentation for the evaluation of non-linear soil response on ground surface motion. *Proceedings of the 11th Structural Mechanics in Reactor Technology Conference*, Tokyo, Japan, August.

Pezeshk S, Zarrabi M (2005). A new inversion procedure for spectral analysis of surface waves using a genetic algorithm. *Bulletin of the Seismological Society of America*, 95(5), 1801-1808.

Rathje EM, Navidi S (2013). Identification of site parameters that improve predictions of site amplification, PEER Report 18; University of California, Berkeley, USA.

Rodríguez-Zúñiga JL, Ortiz-Alemán C, Padilla G (1997). Application of genetic algorithms to constrain shallow elastic parameters using in situ measurements. *Soil Dynamics and Earthquake Engineering*, 16(3), 223-234.

Rokonuzzaman MD, Sakai T (2010). Calibration of the parameters for a hardening-softening constitutive model using genetic algorithms. *Computers and Geotechnics*, 37(4), 573-579.

Sadouki A, Harichane Z, Chehat A (2012). Response of a randomly inhomogeneous layered media to harmonic excitations. *Soil Dynamics and Earthquake Engineering*, 36, 84-95.

Sato T, Yoshida I, Adachi Y (2013). Optimization of seismic sensor locations along highway links. *Journal of Earthquake and Tsunami*, 7(2), 11p.

SHAKE (2000). A computer program for conducting equivalent-linear seismic response analyses for horizontally layered soil deposits, a modified PC version of the original SHAKE program published in 1972 by Schnabel, Lysmer and Seed (modifications made by Idriss IM, Sum JI). EERI, University of California, Berkley, USA.

Steidl JH, Tumarkin AG, Archuleta RJ (1996). What is a reference site?. *Bulletin of the Seismological Society of America*, 86(6), 1733-1748.

Şafak E (1995). Discrete-time analysis of seismic site amplification. *Journal of Engineering Mechanics*, 121(7), 801-809.

Tallett-Williams S, Gosh B, Wilkinson S, Fenton C, Burton P, Whitworth M, Datla S, Franco G, Trieu A, Dejong M, Novellis V, White T, Lloyd T (2016). Site amplification in the Kathmandu valley during the 2015 M7.6 Gorkha, Nepal earthquake. *Bulletin of Earthquake Engineering*, 14, 3301–3315.

Walter E, Pronzato L (1997). Identification of Parametric Model from Experimental Data. Springer-Verlag, London, UK.

Wolf JP (1985). Dynamic Soil-structure Interaction. Prentice-Hall, Inc., Englewood Cliffs, New Jersey, USA.

Zerva A, Harada T (1997). Effect of surface layer stochasticity on seismic ground motion coherence and strain estimates. *Soil Dynamics and Earthquake Engineering*, 16(7), 445-457.

Challenge Journal of Structural Mechanics

Estimating bearing capacity of shallow foundations by artificial neural networks

Mustafa Aytekin *

Department of Civil Engineering & Architecture, University of Bahrain, 32038 Isa Town, Kingdom of Bahrain

ABSTRACT

In this study, the Artificial Neural Network, ANN is applied to data extracted from a large set of random data created by using Terzaghi and Meyerhof formulae. By using MS Excel, 3750 sets of data for Terzaghi's equation, 4000 for Meyerhof's equation were generated. A simulated ANN was trained on a subset of bearing capacity data, and the performance was tested on the remaining data. The performances of the ANN models were compared to Terzaghi and Meyerhof results. ANN models were as accurate as the other techniques in estimating the ultimate bearing capacity. The models estimated the ultimate bearing capacity with an average error of around 1% of the value obtained from Terzaghi and Meyerhof equations, and the coefficient of determination (r^2) was almost equal to 1. Their sensitivity and specificity is dependent on the function and the algorithm used in the training process. Validation subset is crucial in preventing the over-fitting of the ANN models to the training data. ANN models are potentially useful technique for estimating the bearing capacity of the soil. Large training data sets are needed to improve the performance of data-derived algorithms, in particular ANN models.

ARTICLE INFO

Article history:
Received 15 June 2017
Revised 30 August 2017
Accepted 14 November 2017

Keywords:
Bearing capacity
Shallow foundations
Artificial neural networks
Terzaghi's equation
Meyerhof's equation

1. Introduction

Bearing capacity is affected by several parameters and factors such as width and depth of foundation, unit weight of soil, depth of ground water table, friction angle, and cohesion of soil. Due to the complex relationship between the parameters, estimating of ultimate bearing capacity is neither easy nor accurate (Das, 2011; Bowles, 2001). The purpose of this research is to investigate the adequacy of using ANN in estimating ultimate bearing capacity as a new alternative method. The idea was to use a number of field data that are obtained from field tests to develop ANN program that is capable of estimating bearing capacity to avoid the need of field test in the future, but due to lack of field data, Terzaghi and Meyerhof equations have been used to produce data that are used for ANN.

2. Bearing Capacity of Shallow Foundations

Terzaghi expressed well known ultimate bearing capacity of a strip foundation in the form:

$$q_u = cN_c + qN_q + \frac{1}{2}\gamma B N_\gamma \,. \quad (1)$$

The ultimate bearing capacity equation that expressed by Terzaghi did not take into account the shearing resistance along the failure surface in soil above the bottom of the foundation. Also, it assumed the load on the foundation is vertical and axial. However, the load may be inclined. To account for all these shortcomings, Meyerhof (1963) suggested the following form of the general bearing capacity equation:

$$q_u = cN_c F_{cs} F_{cd} F_{ci} + qN_q F_{qs} F_{qd} F_{qi} + \frac{1}{2}\gamma B N_\gamma F_{\gamma s} F_{\gamma d} F_{\gamma i} \,. \quad (2)$$

* *Corresponding author*. Tel.: +973-36936675 ; Fax: +973-17680843 ; E-mail address: maytekin1@gmail.com (M. Aytekin)
ISSN: 2149-8024 / DOI: https://doi.org/10.20528/cjsmec.2017.11.016

Meyerhof introduced more factors for Terzaghi's bearing capacity equation to take into account the various effects that Terzaghi ignored or assumed. Also, tests on laboratory show different results for bearing capacity factors.

3. Artificial Neural Network

The research community started studying the possibility of generating an artificial neural network that is similar to human brain neurons which can be produced through evolutionary algorithms for the last 32 years (Kauffman, 1993). This information processing paradigm is inspired by mimicking the biological nervous systems (Graupe, 2006).

4. Artificial Neural Network Training Program

4.1. Procedure

Due to lack of field data, a set of data were generated using two methods (Terzaghi, and Meyerhof) and bearing capacity was calculated using the equations. By using MS Excel, a set of data were generated (3750 for Terzaghi's equation, 4000 for Meyerhof's equation). The involved parameters were constrained by some limits that Table 1 shows.

Table 1. Limits of bearing capacity parameters.

Parameter	From	To
γ: Unit weight of soil [kN/m^3]	13	21
γ_{sat}: Saturated unit weight of soil [kN/m^3]	13	23
c: Cohesion of soil [kN/m^2]	0	100
D_f: Depth of foundation [m]	0	7
B: Width/Diameter of foundation [m]	0	11
L: Length of foundation [m]	0	40

After generating the input and target data, MATLAB was used to perform ANN training program. Using the ANN main tool "nnstart" seen in Fig. 1, the functions were generated. These functions had simple setups which results in large deviation from the desired values that have been calculated using the theoretical equations, so a need for customized function is required. Due to the complexity of the ANNs and the large amount of parameters involved in the bearing capacity equations, the customized script has to be changed for each case (the three cases of depth of groundwater D_w) and retrained so that a suitable output is achieved. Then, by creating a customized script the training period started.

In the training period, the script that does the training process had to be changed in terms of number of neurons and hidden layers in a trial and error process. It worth mentioning that the use of a large number of neurons will cause two problems, the first one is that the ANN tool will over fit the data on the data that has been used for the training and producing perfect results for them but when new data is tested in the function the output will not match the desired target value. Secondly, a large number of arterial neurons will need a long time and huge processing power of the computer which is unfortunately was not available for us.

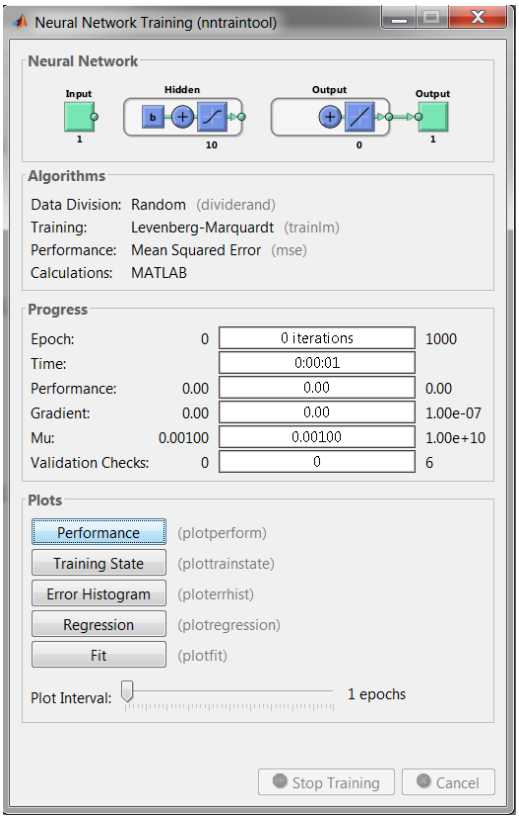

Fig. 1. ANN training progress window.

Thus, as mentioned before a balance between the over-fitting and non-fitting result is required. After finding a suitable number of neurons and hidden layers the retraining process will take place because as the program retained the performance and outputs will get better up to a certain point, after that the program will start to deviate from the intended target.

After finishing the training process, the functions were generated with a small mean squared error values. This conclude the usage of ANN, then a verification of the functions that has been generated using the ANN had been done by using a random set of data to test the functions so the ones with the huge error were excluded and the best were selected. After that, a conclusive data analysis is performed on the functions to find its reliability. The final stage is to use all the functions that has been created and tested to generate a graphical interface that is easy to use and independent of MATLAB and could be used to calculate the ultimate bearing capacity with a high level of confidence.

After performing program training for each case for both equations (Terzaghi and Meyerhof) the generated ANN functions were tested under various conditions and scenarios in order to check the percentage error of the

functions by comparing its results with Terzaghi and Meyerhof equations results before deciding whether the produced function is adequate to be used or not.

The testing process is based on different scenarios. There are three cases according to depth of groundwater D_w. The variation of each parameter involved in bearing capacity equation with the value of ultimate bearing capacity for each case are analyzed by Terzaghi or Meyerhof against ANN. The detailed analyses were performed for strip, square, rectangular and circular foundations of Terzaghi's equations under axial loads while for Meyerhof's equation the analysis have been performed for rectangular/square foundations under axial load as well as under one way eccentricity in x or y directions.

4.2. Analysis of Terzaghi's approach

Fig. 2 shows the results of ultimate bearing capacity comparing the use of the equations against using the ANN model for strip foundation type. It can be noticed from the graph that all points are uniformly distributed on the line indicating that the obtained results from ANN model were excellent. Also, this can be verified numerically as the average percentage error (0.36%) did not exceed 1 with coefficient of determination (r^2) of 1.0.

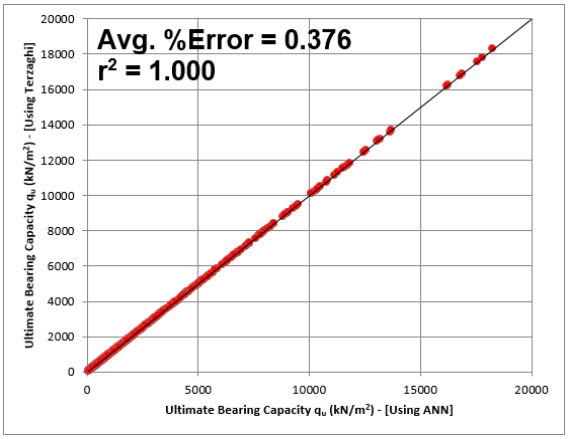

Fig. 2. Comparison between Terzaghi and ANN results for circular foundation.

On the same basis, the results of ANN models for square, rectangular and circular are showed similar behavior. Again, the obtained results were very accurate with average percentage error less than 1% and coefficient of determination (r^2) equal to 1.0.

It is worth mentioning that sometimes the percentage of error jumps dramatically in our analysis but these jumps occur only for very small values of ultimate bearing capacity that is less than 100 kN/m^2 which is impossible to use in project soil, because of the resultant unpredictability of the soil mentioned. Besides, this high percentage error is logical for small values although the difference between values is numerically small which is statistically insignificant. Table 2 shows the average percentage error and coefficient of determination for each type of Terzaghi foundations.

Table 2. Results comparing for Terzaghi ANN models.

Foundation Type	Avg. %Error	r^2
Strip Foundation	0.356	1.000
Square Foundation	0.332	1.000
Rectangular Foundation	0.362	1.000
Circular Foundation	0.376	1.000

4.3. Analysis of Meyerhof's approach

The analysis continues for Meyerhof ANN models as Fig. 3 shows the variation of ultimate bearing capacity for Meyerhof's equation and ANN models for concentric foundation. Similar results were obtained for eccentrically loaded foundations too. Fig. 3 indicates a good distribution of the points on the 45 degree line which means that the results ANN function models produced are matching Meyerhof's equation. It should be noted that average percentage error for Meyerhof's ANN models are a little bit higher than what is obtained for Terzaghi's ANN models although it is still less than 1%, and that because Meyerhof's equation is much more complicated than what Terzaghi described. Meyerhof's equation contains many factors that are approximations or obtained empirically which made life more complicated for ANN model to follow. Despite that, the ANN model for Meyerhof approach is still excellent to use with coefficient of determination (r^2) equal to 1.0. Table 3 shows the average percentage error and coefficient of determination for each type of Meyerhof foundations.

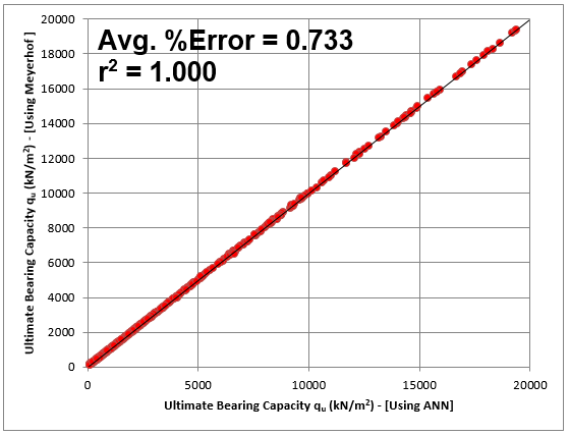

Fig. 3. Comparison between Meyerhof and ANN results for concentric foundation.

Table 3. Results comparing for Meyerhof ANN models.

Foundation Type	Avg. %Error	r^2
Concentric Foundation	0.733	1.000
Eccentric (eB) Foundation	0.622	1.000
Eccentric (eL) Foundation	0.676	1.000

Though in some cases in the detailed analysis the maximum error is large, the coefficient of determination is 1.0 and the average error of all cases is less than 1%, this means that the ultimate bearing capacity computed from the ANN models are following the data calculated from Meyerhof formula and this become obvious when studying the graphs generated from the detailed analysis.

Also from the random data analysis the data are following the 45 degree line meaning that all the values obtained from the theoretical methods and form the ANN models are almost equal. This result in the reinforcement of our findings specifically that the values generated from the ANN models are reliable and accurate enough to be used in estimating the ultimate bearing capacity.

5. Conclusions

This paper proposed a potential solution using an intelligent technique based on ANN to predict the bearing capacities of different types of shallow foundations under various conditions. ANNs were used to simulate the mechanical behavior of soil and more particularly the prediction of the ultimate bearing capacity. The ANNs used were Cascade-forward and Feed-forward neural network were trained with the Bayesian Regularization algorithm.

The performance of the model relies on the training data sets generated. Therefore to have an expert model, a lot of training data sets based on desired results need to be generated. Therefore, a database containing 3750 cases generated through MS-Excel form random generator based on Terzaghi and Meyerhof formulas for ultimate bearing capacity was used for model development and verification. An analysis was carried out to study the relative importance of the factors that affect the ultimate bearing capacity.

The results of the ANN model were compared with the results of the theoretical data which were obtained from the two mentioned traditional methods. The results indicate that the ANN model was capable of accurately simulating the ultimate bearing capacity by using from seven to nine simple parameters as model inputs such as (D_f, B, c, etc.). The results obtained also demonstrate that the ANN method performs as good as the traditional methods with an average percentage error of around 1% of true value obtained from Terzaghi and Meyerhof equations, and coefficient of determination (r^2) almost equal to 1. The neural network model currently demonstrated for this work can be further applied for other theoretical methods as well as field test derived data with various conditions.

A neural network performance depends mostly on its generalization capacity, which in return depends on the data. The study of ultimate bearing capacity variables before the learning process of an ANN model enabled us to determine the importance of the variables on the phenomena. The merits of the neural network are the ability to detect complex nonlinear relationships between dependent and independent variables and to detect the possible interaction between predictor variables and the training algorithms.

ANNs have the advantage that once the model is trained, it can be used as an accurate and quick tool for estimating the total bearing capacity without the need of using tables or charts. The model currently to be developed would increase the efficiency of geochemical design by avoiding complicated and time consuming input file preparation. Thus, neural networks are valuable tools to the soil engineer. An ANN models have been developed for geochemical engineering applications. Also, independent software was produced to ease the calculation of the ultimate bearing capacity for both Terzaghi and Meyerhof.

References

Bowles JE (2001). Foundation Analysis and Design (Third Edition). Peoria, Illinois, USA.

Bullinaria JA (2004). Introduction to Neural Networks. School of Computer Science, The University of Birmingham, Birmingham, UK.

Das BM (2011). Principles of Foundations Engineering. Seventh Edition. Cengage Learning, Stanford, USA.

Dongare AD, Kharde RR, Kachare AD (2012). Introduction to Artificial Neural Network. International Journal of Engineering and Innovative Technology (IJEIT), 2(1), 189-194.

Graupe D (2006). Principles of Artificial Neural Network. World Scientific Publishing, Chicago, USA.

Kauffman SA (1993). Origins of Order. Oxford University Press, New York, USA.

Khashei M, Bijari M (2010). An artificial neural network (p, d, q) model for time-series forecasting. *Expert Systems with Applications*, 37(1), 479-489.

Meyerhof GG (1951). The Ultimate Bearing Capacity of Foundations. Geotechnical Info. Bearing Capacity. Retrieved October 17, 2014.

Challenge Journal of Structural Mechanics

Mechanical and thermal behaviors comparison of basalt and glass fibers reinforced concrete with two different fiber length distributions

Sadık Alper Yıldızel *

Department of Civil Engineering, Karamanoğlu MehmetBey University, 70100 Karaman, Turkey

ABSTRACT

This paper deals with the mechanical and thermal behavior of glass and basalt fiber reinforced concrete. Two different composites were studied containing either basalt or glass fibers. Fiber ratios were selected as 1%, 1.25% and 1.5% for glass fiber; 0.3%, 0.4% and 0.5% for basalt fibers. Fiber length was preferred as 12 mm and 24 mm. The addition of basalt fiber had very limited effect on the compressive, flexure and thermal conductivity properties compared to the glass fiber reinforced composite. The results also showed that composites having fibers with the length of 12 mm had better mechanical properties. Heat transfer simulation of the composites were also conducted. It was obtained that both fibers with the length of 12 mm had very close results on the heat transfer studies.

ARTICLE INFO

Article history:
Received 10 November 2017
Revised 28 November 2017
Accepted 11 December 2017

Keywords:
Glass fiber
Basalt fiber
Fiber reinforced concrete
Mechanical behavior
Heat transfer

1. Introduction

Many researches have been extensively conducted on the mechanical behavior of fiber reinforced concrete due to their wide usage in the construction industry. With the addition of very small amount of fibers, tensile strength and ductility properties of the composites can be enhanced (Alberti et al., 2017; Banthia and Grupta, 2006). There are many fiber types such as glass, basalt, polypropylene and carbon used for this aim (Ivorra et al., 2010).

Among the fiber used for concrete reinforcement, the most common are glass fiber in decorative concrete production. Concrete mixes reinforced with the glass fiber are generally classified as glass fiber reinforced concrete (GFRC). These types of mix designs are widely used in façade, flooring, and sculpturing works (Yıldızel and Ozturk, 2016). Glass fibers enhance the mechanical behavior of the concrete and many academics have been focused on these improvement studies in the last decade (Lv et al., 2012; De Luca et al., 2010; Wei et al., 2010).

Basalt fiber usage in concrete industry has gained popularity due to its mechanical enhancement abilities (Branston et al., 2016). Basalt fiber tensile strength values are higher compared to the glass fibers'. Researches regarding basalt fiber reinforced concrete (BFRC) were mainly focused on mechanical properties of the reinforcing composite materials. Basalt fibers are generally added with the maximum ratio of 0.5 % by volume in the literature studies (Borhan, 2013; Iyer, 2015). However, optimum fiber ratio can be changed for different studies (Ayub et al., 2015). Basalt fibers also enhance the flexural toughness of the concrete (Lipatov et al., 2015).

Basalt fiber production costs are low, these types of fibers can be manufactured under more environment friendly conditions compared to the glass fiber. This paper aims to discuss the potential use of basalt fiber in replacement of glass fiber for decorative concrete production industry.

2. Materials and Experimental Method

Twelve different mixes were designed and prepared within the scope of this study. CEM I 52.5 R Portland type cement was used. The chemical and physical properties of the cement are given in Table 1. Alkali resistant glass fibers and basalt fiber were selected as aggregates. The fiber properties are presented in Table 2.

* *Corresponding author*. Tel.: +90-338-2262000 ; Fax: +90-338-2262214 ; E-mail address: sayildizel@kmu.edu.tr (S. A. Yıldızel)
ISSN: 2149-8024 / DOI: https://doi.org/10.20528/cjsmec.2017.12.017

Table 1. The chemical and physical properties of the cement.

Chemical properties (%)		Physical and mechanical properties	
SiO2	21.60	Specific Weight	3.06
Al2O3	4.05	Specific Surface (cm^2/gr)	4600
Fe2O3	0.26	Whiteness (%)	85.5
CaO	65.70	Initial Setting (min.)	100
MgO	1.30	Final Setting (min.)	130
Na2O	0.30	Water Used for Consistency (%)	30
K2O	0.35	Volume Constancy (mm)	1.0
SO3	3.30	Remnants Obtained Using 0.045 Sieve (%)	1.0
Free CaO	1.60	Remnants Obtained Using 0.090 Sieve (%)	0.1
Chloride (Cl)	0.01	Compressive Strength for 2 days (MPa)	37.0
Insoluble	0.18	Compressive Strength for 7 days (MPa)	50.0
Loss on Ignition	3.20	Compressive Strength for 28 days (MPa)	60.0

Table 2. Basalt and glass fiber properties.

Alkali resistant glass fiber (GF)		Basalt fiber (BF)	
Ultimate strength, bending (MOR, MPa)	20-28	Breaking strength (MPa)	3,200-4,800
Elastic limit (LOP, MPa)	7-11	Modulus of elasticity (GPa)	79 - 92
Compressive strength (MPa)	50-80	Thermal conductivity (W/mK)	0.031-0.038
Modulus of elasticity (GPa)	10-20	Density (kg/m^3)	2650
Thermal conductivity (W/mK)	0.034 – 0.04	Alkali resistant	excellent
Density (kg/m^3)	1870 - 2100		
Alkali resistant	excellent		

Fiber were added into the mixes with the length of 12 mm and 24 mm. Glass fiber were used with the ratio of 1%, 1.25% and 1.5%. Basalt fibers were added as 0.3%, 0.4% and 0.5% in parallel with the similar literature research (Lipatov et al., 2015). Silica sand with the AFS value of 80 to 100 was preferred as the aggregate ingredient in this study. Properties of the sand are given in Table 3.

Table 3. Silica sand properties.

Sieve size	1mm	710 μm	500 μm	355 μm	250 μm	180 μm	125 μm	90 μm	63 μm
Production range (%)	0	0	0	0.2	0.3	20.1	60.4	16.1	1.8
Mean grain size (μm)					140-170				
Clay content (%)					0.6 -0.8				
Specific weight					2.68				
AFS values					84.6				

The third generation polycarboxylate based plasticizer were used as the chemical agent. Water / cement ratio was kept constant at 0.42.

Mix designs and experimental sets are given in Table 4. All prepared specimens were kept at the molds for 24 hours at the room temperature, and potable water was used for the mixes.

5 cm x 5 cm x 5 cm cubic samples for compressive tests, and 27.5 cm x 5 cm x 1.2 cm rectangular samples for flexural tests were prepared according to the TS EN 12467 standard. Compressive and flexural strength of the samples were measured for 1, 7 and 28 days according to the TS EN 1170-4,5 standards. Water absorption and density measurement results were also recorded as per the regulations of TS EN 12467 standard.

Heat transfer simulation of the mixture were analyzed with the aid of the simulation program Energy2D to make further selection of the more compatible composite due to the limited time and material constraints. Simulation results were compared with the similar research test results.

Table 4. The mixture designs.

Mixture Code	Cement (kg)	Sand (kg)	GF (%)	BF (%)	Fiber Length (mm)	W / C
GFM-1	50	50	1.00	-	12 mm	0.42
GFM-2	50	50	1.25	-	12 mm	0.42
GFM-3	50	50	1.50	-	12 mm	0.42
GFM-4	50	50	1.00	-	24 mm	0.42
GFM-5	50	50	1.25	-	24 mm	0.42
GFM-6	50	50	1.50	-	24 mm	0.42
BFM-1	50	50	-	0.30	12 mm	0.42
BFM-2	50	50	-	0.40	12 mm	0.42
BFM-3	50	50	-	0.50	12 mm	0.42
BFM-4	50	50	-	0.30	24 mm	0.42
BFM-5	50	50	-	0.40	24 mm	0.42
BFM-6	50	50	-	0.50	24 mm	0.42

3. Results and Discussions

Mechanical properties of the composites were presented in this section. The compressive and flexural test results of the specimens are given in Figs. 1 and 2, respectively.

Compressive test results showed that compressive strength values increase with the increasing fiber ratios. Mixture design GFM-3 had the highest compressive strength value as 36.43 MPa for 28 days. BFM-3 with the basalt fiber ratio of 0.5 % had close compressive strength value compared to the glass fiber reinforced composites. Fiber length factor also effected the compressive strength values. Mix design with the fiber length of 12-mm showed better performances compared to the 24-mm fiber added composites, as seen in Fig. 1.

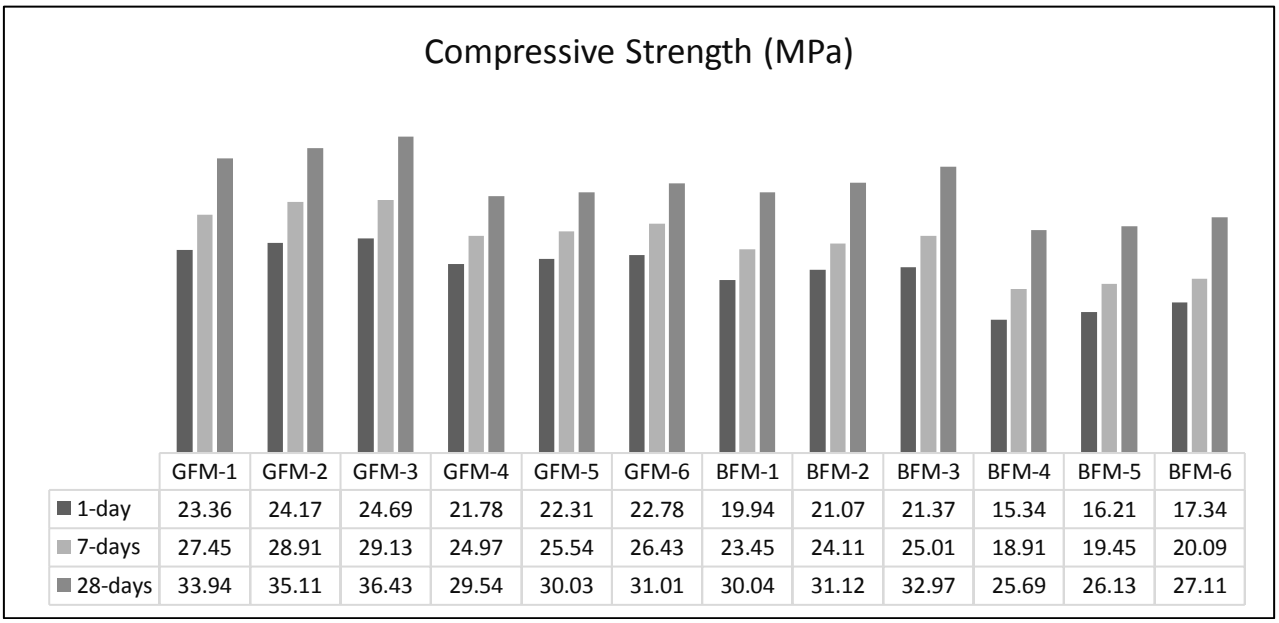

	GFM-1	GFM-2	GFM-3	GFM-4	GFM-5	GFM-6	BFM-1	BFM-2	BFM-3	BFM-4	BFM-5	BFM-6
1-day	23.36	24.17	24.69	21.78	22.31	22.78	19.94	21.07	21.37	15.34	16.21	17.34
7-days	27.45	28.91	29.13	24.97	25.54	26.43	23.45	24.11	25.01	18.91	19.45	20.09
28-days	33.94	35.11	36.43	29.54	30.03	31.01	30.04	31.12	32.97	25.69	26.13	27.11

Fig. 1. Compressive strength test results.

Flexural strength values increased with the increase in fiber ratios. The mix GFM-3 had the highest strength value as seen in Fig. 2. As expected, the flexural strength values are increased with the increasing fiber ratio 12-mm length fiber added composite showed better performance for both fiber types. The mix BFM-3 had similar mechanical performance compared to the glass fiber reinforced concrete test results.

Water absorption (%) and density measurement results are given in Fig. 3. Water absorption values increases with the increasing pore ratio of the samples. In other words, water absorption percentages decrease with the increase in density values.

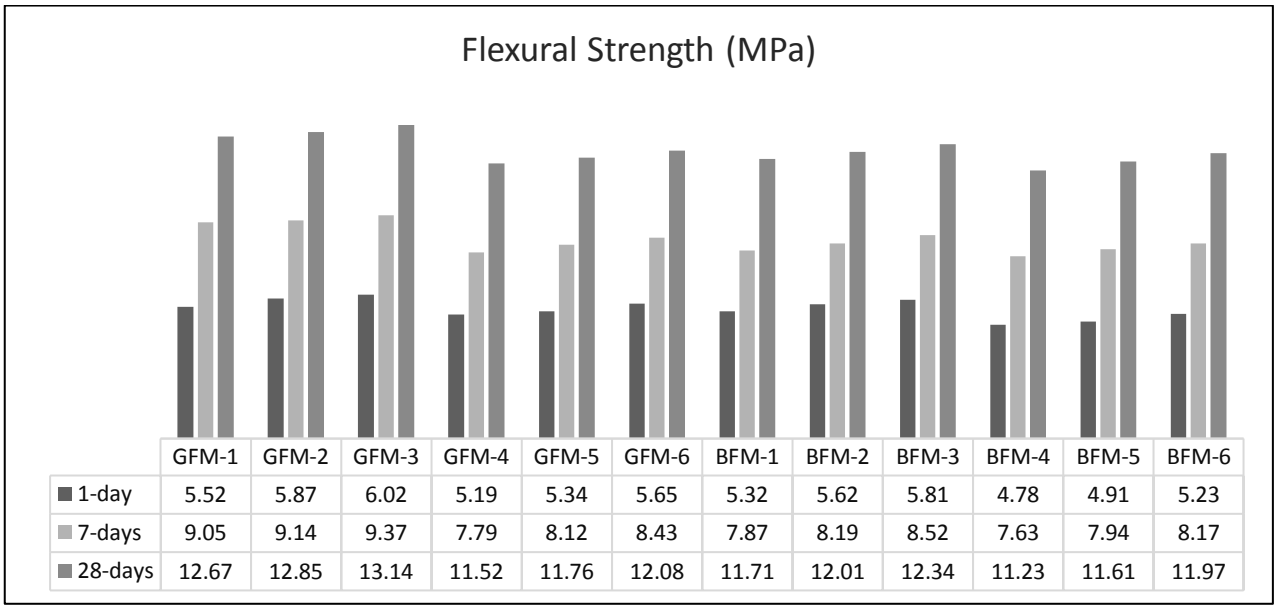

	GFM-1	GFM-2	GFM-3	GFM-4	GFM-5	GFM-6	BFM-1	BFM-2	BFM-3	BFM-4	BFM-5	BFM-6
1-day	5.52	5.87	6.02	5.19	5.34	5.65	5.32	5.62	5.81	4.78	4.91	5.23
7-days	9.05	9.14	9.37	7.79	8.12	8.43	7.87	8.19	8.52	7.63	7.94	8.17
28-days	12.67	12.85	13.14	11.52	11.76	12.08	11.71	12.01	12.34	11.23	11.61	11.97

Fig. 2. Flexural strength test results.

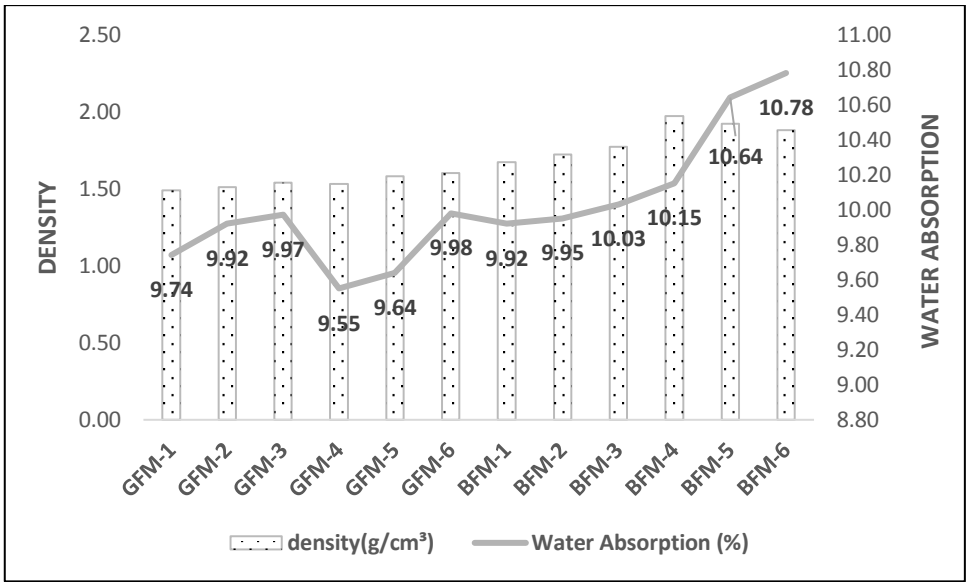

Fig. 3. Water absorption (%) vs density (g/cm^3).

Thermal behavior of the fiber added composites were analyzed via Energy2D software. The heat transfer properties of the GFM-3 and BFM-3 composites were simulated due to their superior mechanical behaviour compared to the other mixes. Heat transfer rate of the composites were simulated at the temperature value of –30°C and +60°C. Material thermal bridge method was used. The simulation results were given in Figs. 4-7 respectively.

Simulation result showed that GFM-3 and BFM-3 showed very similar performance on heat transmission values. Results are the same as 0.17 W/m^2 for both mixes at the temperature of –30°C. Additionally, simulation results vary from 0.34 W/m^2 to 0.3 W/m^2 at 60°C.

4. Conclusions

Glass and basalt fiber reinforced composites were analyzed and compared for the mechanical and heat transfer rate properties. The main findings can be summarized as follows:

- The increase in fiber ratio for glass fibers up to 1.5% and for basalt fibers up to 0.5% in composites designs increases the compressive and flexural test results of the mixes.
- Glass fiber added composites showed better performances when analyzing flexural and compressive strength test results with the fiber ratio of 1.5%. However, basalt fiber reinforced concrete had very similar results with fiber ratio of 0.5%.

- Fiber length of 12-mm showed better test results for all types of fibers compared to the 24mm fiber added mixes.
- Heat transfer simulation results of the both fiber types were very close as 0.34 W/m² to 0.3 W/m² at 60°C.
- Addition of 1.5% glass fiber presents the best mechanical results for the fiber reinforced composites.
- Water absorption values decreased with the increase in the density values of the composites. Basalt fiber reinforced mixes can be strengthened with a filler material to obtain more impermeable composite material.

In the light of abovementioned results, basalt fibers can be used as replacement of glass fiber due to their low cost and very similar performances in concrete composite applications.

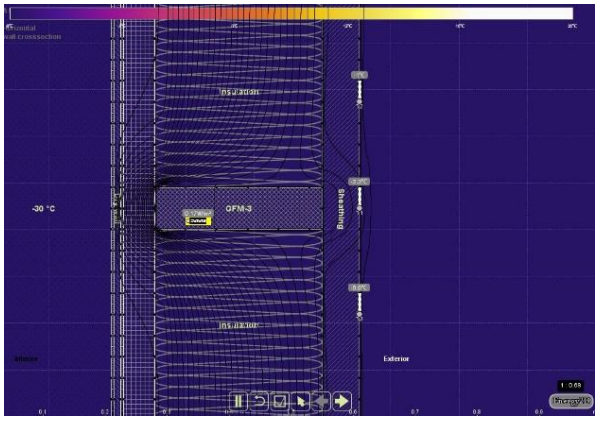

Fig. 4. GFM-3 (Sim:1@-30°C).

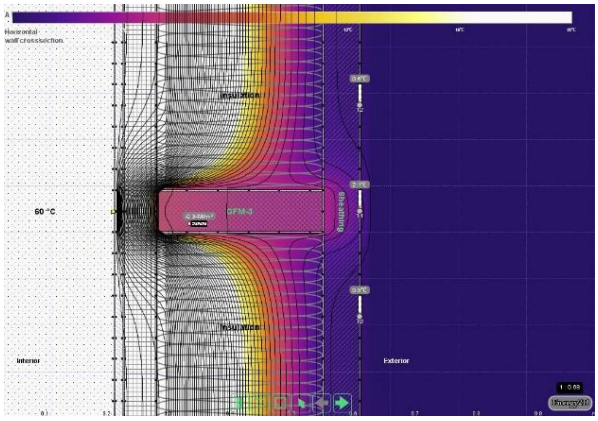

Fig. 5. GFM-3 (Sim:2@60°C).

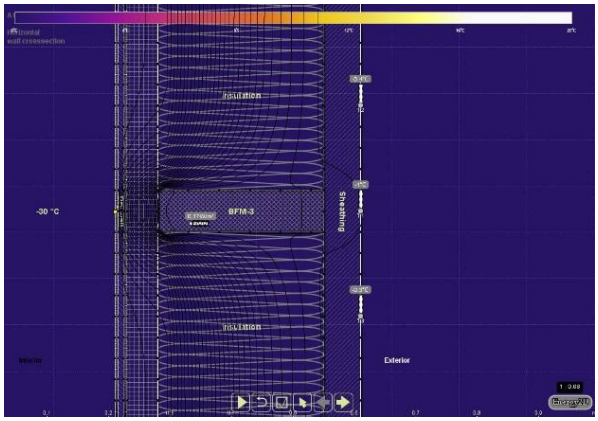

Fig. 6. BFM-3 (Sim:3@-30°C).

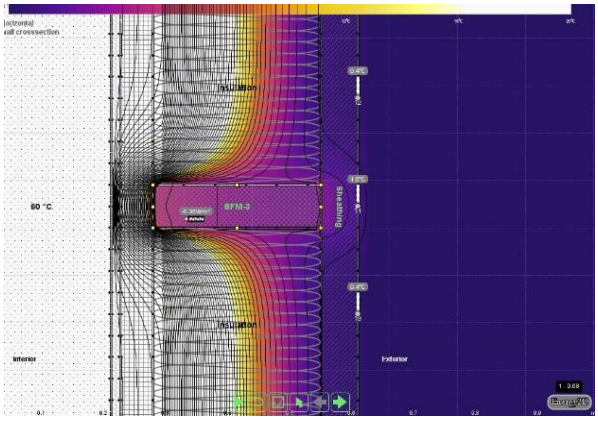

Fig. 7. BFM-3 (Sim:4@60°C).

REFERENCES

Alberti MG, Enfedaque A, Gálvez JC (2017). Fibre reinforced concrete with a combination of polyolefin and steel-hooked fibres. *Composite Structures*, 171, 317-325.

Ayub T, Shafiq N, Nuruddin MF (2014). Mechanical properties of high-performance concrete reinforced with basalt fibers. *Procedia Engineering*, 77, 131-139.

Banthia N, Gupta R (2006). Influence of polypropylene fiber geometry on plastic shrinkage cracking in concrete. *Cement and Concrete Research*, 36(7), 1263-1267.

Borhan TM (2013). Thermal and mechanical properties of basalt fibre reinforced concrete. *In Proceedings of World Academy of Science, Engineering and Technology (WASET)*, 76, 313.

Branston J, Das S, Kenno SY, Taylor C (2016). Mechanical behaviour of basalt fibre reinforced concrete. *Construction and Building Materials*, 124, 878-886.

De Luca A, Matta F, Nanni A (2010). Behavior of full-scale glass fiber-reinforced polymer reinforced concrete columns under axial load. *ACI Structural Journal*, 107(5), 589.

Ivorra S, Garcés P, Catalá G, Andión LG, Zornoza E (2010). Effect of silica fume particle size on mechanical properties of short carbon fiber reinforced concrete. *Materials & Design*, 31(3), 1553-1558.

Iyer P, Kenno SY, Das S (2015). Mechanical properties of fiber-reinforced concrete made with basalt filament fibers. *Journal of Materials in Civil Engineering*, 27(11), 04015015.

Lipatov YV, Gutnikov SI, Manylov MS, Zhukovskaya ES, Lazoryak BI (2015). High alkali-resistant basalt fiber for reinforcing concrete. *Materials & Design*, 73, 60-66.

Lv Y, Cheng HM, Ma ZG (2012). Fatigue performances of glass fiber reinforced concrete in flexure. *Procedia Engineering*, 31, 550-556.

Wei B, Cao H, Song S (2010). Tensile behavior contrast of basalt and glass fibers after chemical treatment. *Materials & Design*, 31(9), 4244-4250.

Yıldızel SA, Öztürk AU (2016). A study on the estimation of prefabricated glass fiber reinforced concrete panel strength values with an artificial neural network model. *CMC: Computers, Materials & Continua*, 52(1), 42-51.

Challenge Journal of Structural Mechanics

Structural behaviour of concrete filled hollow steel sections exposed to parametric fire

Mohammed Salah Dimia [a,*], Soumia Sekkiou [a], Mohamed Baghdadi [a], Mohamed Guenfoud [b]

[a] *Department of Civil Engineering, University of Batna 2, 05000 Batna, Algeria*
[b] *Department of Civil Engineering, 8 Mai 1945 University of Guelma, BP.401, 24000 Guelma, Algeria*

ABSTRACT

This article analyzes steel-concrete composite columns subjected to natural fire scenarios in order to verify that the possibility of structural collapse during or after the cooling phase is real. The main objectives of this study are: first, to highlight the phenomenon of delayed collapse of this type of columns during or after the cooling phase of a fire, and then analyze the influence of some determinant parameters, such as section size, tube thickness, reinforcement (ratio), concrete cover and column length. The results show that critical conditions with respect to delayed failure arise for massive sections, small values of the steel tube thickness and for columns with massive section.

ARTICLE INFO

Article history:
Received 25 December 2016
Accepted 24 February 2017

Keywords:
Natural fire
Fire resistance
Composite column
Cooling phase
Residual strength

1. Introduction

The fire behavior of composite columns and especially concrete filled hollow steel sections has been studied extensively in various countries, while studying almost all essential parameters identified: section shape and dimensions (Dai and Lam, 2012), concrete filling (Dotreppe et al., 2010), reinforcement rate, steel tube thickness, column slenderness (Ana et al., 2012), thermal and mechanical properties of steel and concrete (Sangdo and Amit, 2009), and even the contact problem at the steel-concrete interface (Zhong et al., 2011). Most of this works were done under standard fire conditions (ISO). However, if the behavior of a structure is evaluated by means of a performance-based approach, a more realistic representation of the fire should be used, and we must ensure for the entire duration of fire an acceptable risk of failure under the effect of natural fire. The influence of such realistic fire scenarios in the evaluation of the fire resistance is a key issue in the performance-based approach, as presented for example by Fike and Kodur (2009) for concrete-filled hollow structural section columns. The required duration of stability may be longer than the duration of the heating phase; it may even be required that the structure survives the total duration of the fire until complete burnout.

Under real fire conditions, the stability of the structural element or the entire structure must necessarily be performed in the entire time domain by a step by-step iterative method. Some authors have been interested in the residual load bearing capacity of structural elements after exposure to fire, for example Han et al. (Han et al., 2002) for composite columns, and they even developed formulas for calculating the index of the residual strength.

However, structural failure that would occur at a later stage, may be an even greater threat because it would occur at the time of first inspection, not only by the fire brigades but also possibly by other people. Such a tragic incident occurred in Switzerland in 2004. It's also occurred this type of collapse during the cooling phase of a fire in a full-scale fire test conducted in 2008 by Wald (Wald and Kallerova, 2008) in the Czech Republic.

These events show the need to conduct detailed studies on the risk of delayed collapse of structures in natural fire. The evolution of material properties in the cooling phase must be available to perform such analysis. The authors' previous work on the subject has lead them to the conclusion that, for concentrically loaded simply supported concrete columns heated on three sides, a delayed collapse is a possible event (Jernay and Dimia,

* *Corresponding author*. Tel.: +213-69-8945096 ; Fax: +213-33-230206 ; E-mail address: ms.dimia@univ-batna2.dz (M. S. Dimia)
ISSN: 2149-8024 / DOI: https://doi.org/10.20528/cjsmec.2017.02.004

2011; Dimia et al., 2011). This previous work was conducted using the generic constitutive models of Eurocode for steel and for concrete, for the reason that these models are widely accepted by the scientific community and typically used for structural analyses.

This article analyzes steel-concrete composite columns subjected to natural fires in order to verify that the possibility of structural collapse during or after the cooling phase is real and, if so, what the parameters and conditions are that more likely lead to this undesirable behavior.

2. Analysis Procedure

A sequentially coupled thermo-mechanical analysis is used to carry out the numerical simulations. The nonlinear finite element software SAFIR developed at the University of Liege (Franssen, 2010) for the simulation of structures subjected to fire was used. The analysis was performed by first conducting a pure heat transfer analysis for computing the temperature field and afterwards a stress/deformation analysis for calculating the structural response. The discretization for plane sections of different shapes is possible by using triangular and/or quadrilateral elements. For each element the material can be defined separately. Any material can be analyzed, provided that its thermal and physical properties at elevated temperatures are known. The variation of material properties with temperature can be considered.

2.1. Thermal analysis

The temperature curves considered as input data were taken from the parametric fire model of Annex A (A.2 a) in Eurocode 1 pat 1-2 (EC1, 2002), that represents the action of a natural fire including the cooling phase. The factor Γ that appears in Eq. (A.2 a) was given the value of 1.0, which makes the heating phase of the time temperature curve of this natural fire model very close to the standard curve as shown in Fig. 1. A uniform temperature has been assumed over the height of the column. The temperature distribution in the sections was determined by 2D nonlinear transient analyses, an example of temperature distribution inside a typical column section is shown in Fig. 2.

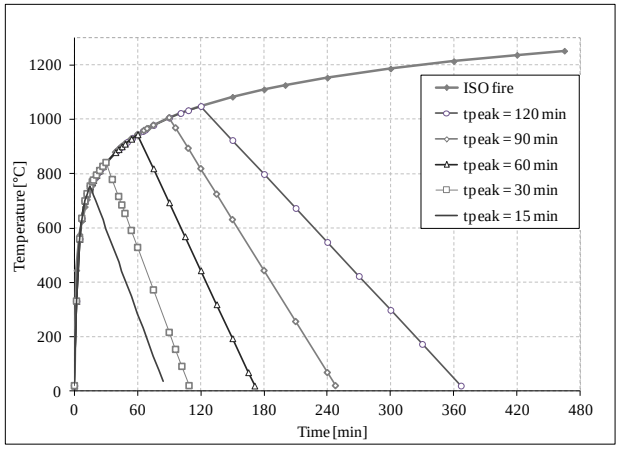

Fig. 1. Fire curves considered in the parametric analyses.

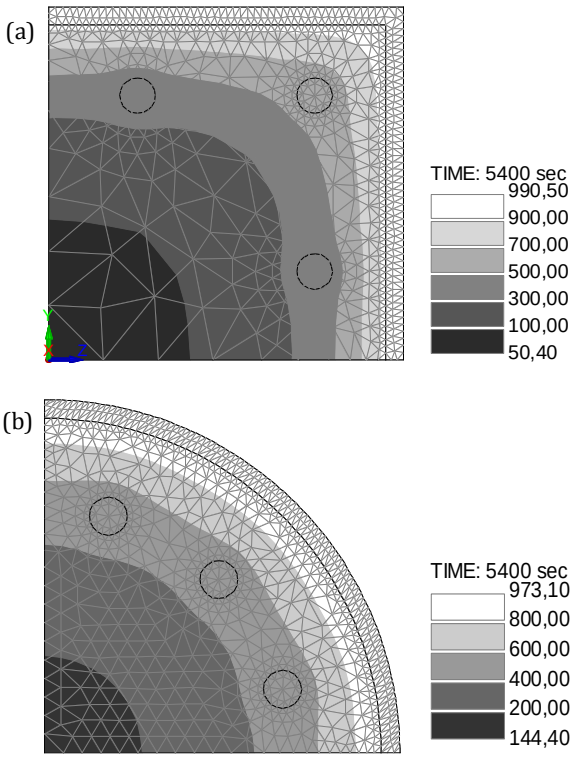

Fig. 2. Isotherms after 90 min in a section heated on four sides (1/4 modeled): (a) S400x10; (b) C300x8.

The non-steady-state 2D temperature distribution within any cross-section is determined by Fourier's equation:

$$k\left(\frac{\partial^2 T}{\partial x^2}+\frac{\partial^2 T}{\partial y^2}\right)+Q=p.c.\frac{\partial T}{\partial t}, \quad (1)$$

where k is the thermal conductivity of the material, T is the temperature, Q is the amount of heat generated in the material per unit volume, ρ is the density, c is the specific heat, t is the time, and x, y are spatial coordinates in the plane of the cross section. The temperature fields within a given section are evaluated by means of a finite element analysis in conjunction with an integration method for time steps.

2.2. Structural analysis

The columns were discretized longitudinally by means of Bernoulli beam type elements and the cross sections of the beam elements are divided into fibers that match the 2D elements of the thermal analysis.

In the model, a whole composite column is built up by means of several 2-D beam elements which are based on the following formulations and hypotheses:

- The displacement of the node line is described by the displacements of three nodes, two nodes at each end of the element supporting two translations and one rotation in plane plus one node at mid-length supporting the non-linear part of longitudinal displacement.
- The Bernoulli hypothesis is considered, i.e. plane cross sections remain plane after deformation;
- The hypothesis of Von Karman is used : the strains are small;

- The rotations are assumed to be small (note that they are evaluated in the co-rotated configuration);
- The longitudinal integrations are numerically calculated using Gauss' method;
- The integration of the longitudinal stresses and stiffness on the section is based on the fiber model;
- The mechanical interaction between the steel tube and concrete infill was modelled as perfect i.e. no slip occurs at the steel-concrete boundary
- A sinusoidal imperfection with maximum amplitude [Dotreppe et al., 2010) has been introduced in the direction of the thermal gradient (leading to bending along one single axis).
- D/th is less than $52 = \sqrt{235/f_y}$ (D: the outside dimension of the columns, th: the thickness of the steel tube) to neglect the effect of local buckling in the steel wall according to Eurocode 4-Part 1.1 (EC4, 2004).

3. Material Models at Elevated Temperatures

The numerical model takes into account the temperature-dependent thermal and mechanical properties of the materials.

3.1. Thermal models

The thermal properties of steel and concrete in the heating phase have been taken from EN1994-1-2 (EC4, 2005). This means that thermal conductivity of concrete was taken with the upper limit in the sense of EN 1992-1-2 (EC2, 2004). Siliceous concrete was chosen, with a density of 2300 kg/m^3 and a water content of 92 kg/m^3. As previously mentioned the thermal boundary conditions consist of thermal radiation and forced convection. The thermal radiation is defined by the steel emissivity which is taken equal to 0.7, whereas the forced convection is taken equal to 35 W/m^{2}K. Thermal properties of steel were considered as fully reversible during cooling. The specific mass of concrete, which decreases during heating because of the release of water, has been considered as constant during cooling. When the temperature increases in the concrete, the thermal conductivity has a tendency to decrease (EC4, 2005). It keeps the value corresponding to the maximum temperature during cooling.

3.2. Mechanical models

The mechanical properties of the steel have been considered as reversible, which means that stiffness and strength are recovered to full initial values during cooling. In the thermal elongation curve, the plateau corresponding to the phase change that occurs around 800°C at a level of 11 x 10^{-3} during heating occurs at slightly lower temperatures, around 700°C, at a level of 9 x 10^{-3} during cooling. When steel is back to ambient temperature, there is no residual thermal expansion.

For concrete, a residual thermal expansion or shrinkage has been considered when the concrete is back to ambient temperature. The value of the residual value is a function of the maximum temperature and is taken from experimental tests made by Schneider in 1979 and mentioned in (Schneider, 1985).

Compressive strength of concrete does not recover during cooling. According to EN 1994-1-2, an additional loss of 10% has been considered during cooling. This means that, for example, if the compressive strength has decreased from 1.00 to 0.50 at a given temperature, it will decrease to 0.45 when cooling back to ambient temperature. This assumption is of course the key for all the predictions presented in this paper and thus the reliability of the conclusions. In the stress-strain relationship of concrete, the strain corresponding to the peak stress during cooling is considered fixed to the value that was attained at the maximum temperature Fig. (C.2) of Eurocode 4.

4. Parametric Studies

The main parameters affecting the fire resistance of at elevated temperatures have been investigated). The parameters studied are the outside dimension of HSS columns (D), the thickness of the steel tube (th), the length of column (L), the amount of steel reinforcement (As) and the duration of the heating phase tpeak.

The values that are considered in the parametric analyses are given below:

The outside dimension of the columns (D), the amount of steel reinforcement, the duration of the heating phase does not exceed 120 minutes and the wall thickness. Concrete cover has been fixed at a minimum value of 30 mm. The relative slenderness values of the columns at room temperature were calculated in accordance with Clause 6.7.3.3 of EN 1994-1-1 (EC4, 2004) assuming hinged end conditions.

5. Influence of the Duration of the Heating Phase

Fig. 3 summarizes the analyses performed to examine the influence of the duration of the fire. Each curve is related to one of the fires shown in Fig. 1 and is the result of numerous simulations performed with different load levels. From the load bearing capacity at time t=0, here 5066 kN, the load has been progressively reduced and numerous simulations have been performed, each one for a different load, yielding a fire resistance time that increases as the load is decreased. In a real building, the columns are subjected to different loads, the level of which is not known to the fire fighters. What each curve shows is that, for the curve marked as t_{peak}=30 min for example, if a column is subjected to a load of 2000 kN, it will fail after 40 min. Each of these curves shows whether there is a potential dangerous range of the load that could lead to collapse during or after the heating phase. If this is the case, the fact that a delayed collapse will occur or not in a building will depend on the actual load level on the columns.

It is thus possible, according to this model, to have in certain cases a structural collapse some time after the end of heating phase.

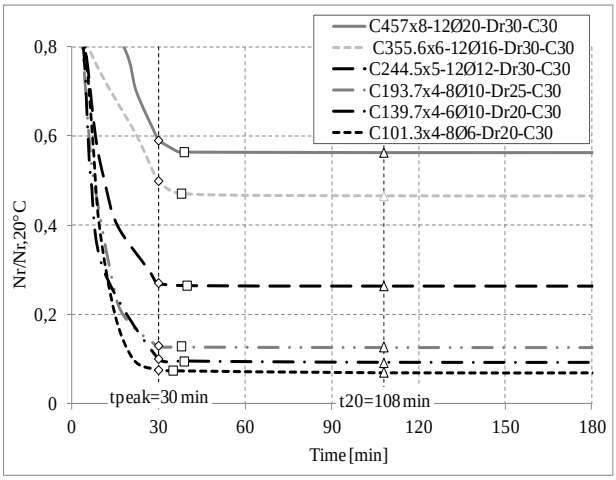

Fig. 3. An example of evolution of the load bearing capacity for a column subjected to natural fire, t_{peak}=30min.

6. Influence of the Section of the Column

The outside dimension of the columns (D) considered are: Square section: S150x4-4Ø12-Dr25-C30, S200x5-12Ø10-Dr25-C30, S300x6-12Ø16-Dr30-C30, S400x10-12Ø20-Dr30-C30 and S500x10-12Ø25-Dr30-C30. Circular section: C139.7x4-6Ø10-Dr20-C30, C193.7x4-8Ø10-Dr25-C30, C244.5x5-12Ø12-Dr30-C30, C355.6-6-12Ø16-Dr30-C30 and C457-8-12Ø20-Dr30-C30.

Each section was exposed to different fires represented on Fig. 1.The analyses have been repeated for different section dimensions of the column with a length of 4m. Fig. 4 shows the peak temperature at various depths of cross section (S400x10-12Ø20-Dr30-C30) to the parametric fires for 30 and 90 min. compared with the temperatures at the end of heating. It can be seen that the grater the depth of concrete, the grater the temperature increase during and after the cooling phase.

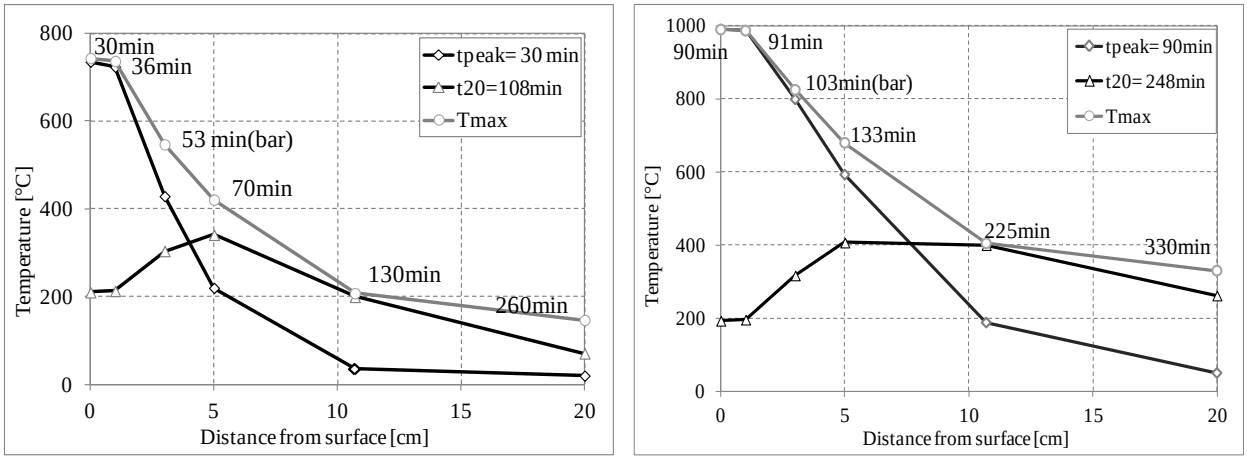

Fig. 4. Evolution of temperatures in a section S400x10-12Ø20-Dr30-C30: (a)- Evolution des T° sous t_{peak}=30min; (b) Evolution des T° sous t_{peak}=90min.

Fig. 5 summarizes the results of the analysis performed on the basic column (4m length) with different shapes for a natural fire with different duration of heating. The curve that gives the evolution of the load bearing capacity is the result of numerous simulations performed with different load levels. From the load bearing capacity at time t=0, the load has been progressively reduced and numerous simulations have been performed. The obtained relationship between the applied load and the fire resistance time gives us the evolution of the load bearing capacity of columns. The load bearing capacity continues decreasing after the maximum gas temperature is reached in the compartment. As can be seen, these curves can be considered as the resistance curves for studied columns corresponding to the lowed load witch the column would support during the fire time. The load bearing capacity continues decreasing after the maximum gas temperature is reached in the compartment.

7. Influence of the Steel Tube Thickness

For a section of 300x300 with different values of the thickness of the steel tube, a collapse, in the cooling phase exists for the majority of the columns studied, and the most critical situations in respect of this late failure arise for small thicknesses for small values of the thickness like it presented on Fig. 6. For the short fire with 30 minutes of heating, we observe the insensitivity of $t_{collapse}$ to the steel tube thickness, for example for a thickness of 4mm , collapse occurs at 12 minutes from the beginning of cooling phase. The same situation is observed for t_{peak}=60minutes, when failure occurs at about 16minutes after the start of cooling. So for short and medium fires (heating between 30 and 60 minutes), the steel tube thickness has almost no influence on the value of $t_{collapse}$. The phenomenon of delayed collapse is more pronounced for small thicknesses, and the $t_{collapse}$ decreases by increasing the thickness until closer to t_{peak}.

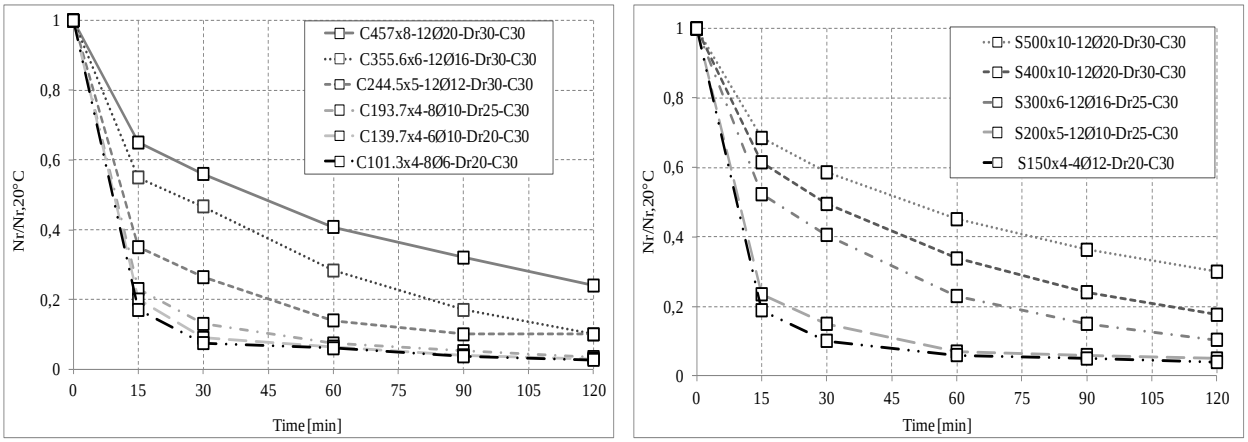

Fig. 5. Evolution of the load bearing capacity for columns subjected to natural fires.

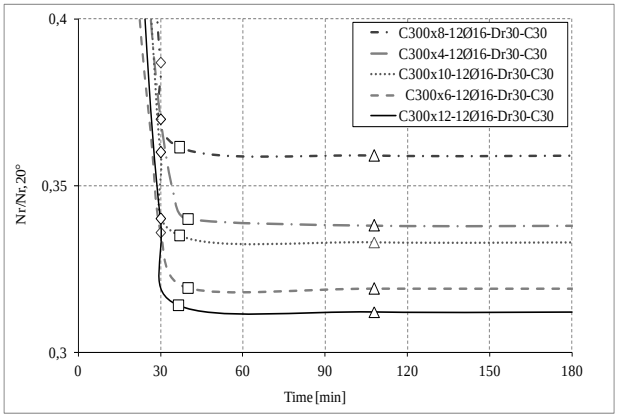

Fig. 6. Influence of the steel tube thickness, t_{peak}=30min.

This can be explained by the fact that increasing the thickness of the steel tube reduces the size of the concrete core which is element responsible for the delayed failure. So a smaller wall thickness implies a larger section of the concrete and therefore more risk of delayed collapse and vice versa.

8. Influence of Reinforcement Rate

Fig. 7 shows clearly a delayed failure for the section S260x7-Dr30 with different reinforcement rates under fire t_{peak}=30min. It occurs about 10 min after the start of the cooling phase. Increasing the amount of reinforcement slightly increases the duration of the $t_{collapse}$. The influence of reinforcement rate on the time of collapse becomes more pronounced when the heating time increases to 60 and 90 minutes. When t_{peak} rises to 90 minutes, increasing the reinforcement section increase the $t_{collapse}$ of an average of about 1 minute/1%, until at *As* = 3.8% a jump in the value of $t_{collapse}$ of the order of 7 minutes compared with the previous value.

Arrive at a percentage of 7.5%, the value of $t_{collapse}$ becomes constant and insensitive to the change of reinforcement. So increasing the reinforcement section increases the concrete resistance and thereby retards columns failure. However, for a heating of two hours, the delayed failure exists 35 minutes after the start of cooling, but the reinforcement rate will have almost no influence on the duration of fire resistance of the element. Fig. 8 shows the fire resistance curve of columns depending on the reinforcement rate.

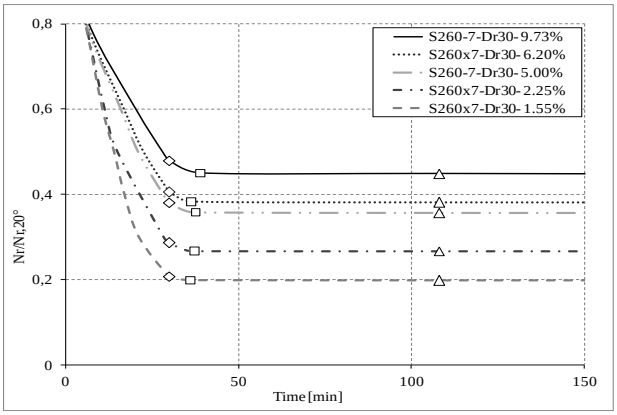

Fig. 7. Influence of the reinforcement rate.

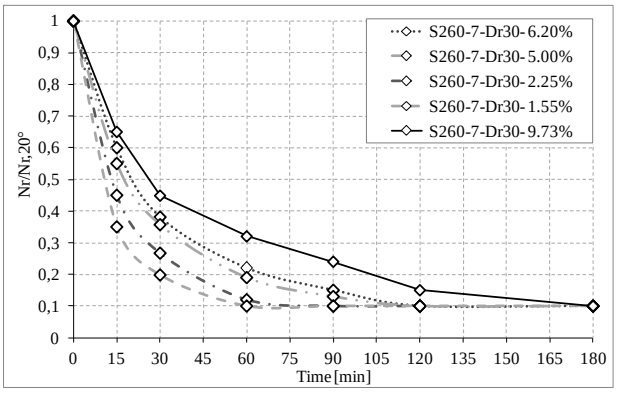

Fig. 8. Fire resistance curves for a column S260x7-Dr30 with different reinforcement rates.

9. Conclusions

A numerical model has been used in this study for concentrically loaded composite steel-concrete columns heated on four sides to highlight the phenomenon of delayed collapse of this type of columns during or after the

cooling phase of a fire. The results show that a failure during the cooling phase of a fire is a possible event even after several minutes after the end of the heating phase.

The main mechanisms for these delayed failures are to be found in the fact that temperatures in the central zones of the concrete core can keep on increasing even after the gas temperature is back to ambient and also in the fact that concrete may lose additional strength during cooling compared to the situation at maximum temperature.

Parametric studies were carried out by means of this numerical model in order to investigate the main parameters affecting directly this delayed collapse of composite columns under natural fire.

It has been shown that the most critical situations with respect to delayed failure arise for short fires, for columns with massive section, for columns with small values of the thickness of the steel tube and for concrete cores with important reinforcement rate.

REFERENCES

Ana E, Manuel LR, Antonio H (2012). Simple calculation model for evaluating the fire resistance of unreinforced concrete filled tubular columns. *Engineering Structures*, 42, 231-244

Dai XH and Lam D (2012). Shape effect on the behaviour of axially loaded concrete filled steel tubular stub columns at elevated temperature. *Journal Constructional Steel Research*, 73, 117-127.

Dimia MS, Guenfoud M, Gernay T, Franssen JM (2011). Collapse of concrete columns during and after the cooling phase of a fire. *Journal of Fire Proection Engineering*, 2(4), 245–263,

Dotreppe JC, Binh TC, Franssen JM (2010). Steel hollow columns filled with self-compacting concrete under fire conditions. *3rd fib International Congress*.

EN 1991-1-2 (2002). Eurocode 1: *Actions on structures-Part 1-2: General actions-Actions on structures exposed to fire. Brussels*: CEN.

EN 1992-1-2 (2004). Eurocode 2: *Design of concrete structures-Part 1-2: General rules-Structural fire design*. Brussels: CEN.

EN 1994-1-1 (2004). Eurocode 4-*Design of composite steel and concrete structures. Part 1-1: General rules and rules for buildings*. Brussels: CEN.

EN 1994-1-2. Eurocode 4 (2005): *Design of composite steel and concrete structures. Part 1-2: General rules – Structural fire design*. Brussels: CEN.

Fike RS and Kodur VKR (2009). An approach for evaluating the fire resistance of CFHSS columns under design fire scenarios. *Journal of Fire Protection Engineering*, 19(4), 229-259.

Franssen J-M (2005). SAFIR: A thermal/structural program for modeling structures under fire. *Engineering Journal*. 42(3), 143-158.

Gernay T, Dimia MS (2011). Structural behavior of concrete columns under natural fires including cooling down phase. *In H. Barros, Faria R, Pina C & Ferreira C (Eds.), Proceedings of The International Conference on Recent Advances in Nonlinear Models - Structural Concrete Applications,*637-656. Portugal: RAGRAF.

Han L-H, Yang Y-F, Yang H, Huo J (2002). Residual strength of concrete-filled RHS columns after exposure to the ISO-834 standard fire. *Thin-Walled Structures,* 40, 991–1012.

Sangdo H, Amit HV (2009). Analytical modeling of the standard fire behavior of loaded CFT columns. *Journal of Constructional Steel Research,* 65, 54-69.

Schneider U (1985). Properties of materials at high temperatures: *Concrete. RILEM*. University of Kassel.

Tao Z, Han L-H, Uy B, Chen X (2011). Post-fire bond between the steel tube and concrete in concrete-filled steel tubular columns. *Journal Constructional Steel Research,* 67, 484-496.

Wald F, Kallerova PD (2008). Summary of results from fire test in Mokrsko. Prague.